Theses

5-10-2024

Unraveling the Role of Asymmetry in Structural Porous Media on the Growth of Fluid Fingers

Amir Ibrahim
ami7627@rit.edu

Follow this and additional works at: https://repository.rit.edu/theses

Unraveling the Role of Asymmetry in Structural Porous Media on the Growth of Fluid Fingers

by

Amir Ibrahim

A Thesis Submitted in Partial Fulfillment of the Requirements for the

Degrees of Master of Science in Materials Science and Engineering and

Bachelor in Physics

School of Physics and Astronomy

School of Chemistry and Materials Science

College of Science

Rochester Institute of Technology

May 10, 2024

Advisors: Shima Parsa, Pratik Dholabhai, Jairo Diaz, Scott Williams

Committee Approval:

_____

Dr. Scott Williams, Ph.D.   Date
Director, Materials Science and Engineering Graduate Program

_____

Dr. Shima Parsa, Ph.D.   Date
Advisor

_____

Dr. Jairo A. Díaz, Ph.D.   Date
Committee Member

_____

Dr. Pratik Dholabhai, Ph.D.   Date
Committee Member

Abstract

Instabilities at fluid-fluid interfaces are ubiquitous in porous media, even at small flow rates. The growth of fluid fingers during fluid-fluid immiscible displacement in a porous medium results in partial saturation of the medium, and inefficiency in displacement has a tremendous economic impact on oil recovery, chemical reactors, and water filtration industries. In this study, we demonstrate that an inherent asymmetry in the structure of a porous medium controls the development of fluid fingers due to instabilities at fluid interfaces. We construct a 2D porous medium consisting of a matrix of triangles using soft lithography to investigate air displacement by water. Utilizing optical microscopy and precise control of the injection pressure, we illustrate that the direction of injection with respect to the orientation of the triangles (apex vs. base) dictates the development of fluid fingers at the interface. At a critical injection pressure, we observe a uniform displacement of air in the apex direction. In contrast, a distinct fluid finger grows when injecting water in the opposite direction (base of the triangle). In this research, we demonstrate that the asymmetry of a porous medium controls the first-order instability at air-water interfaces, leading to the development of fluid fingers.

Table of Contents

List of Figures

List of Tables

1.0 Introduction

In a porous medium, fluid-fluid displacement is controlled by the balance between capillary and viscous pressure. Flow occurs when the invading fluid's viscous force overcomes the capillary forces at the interface of the invading and defending fluids [1]. The capillary forces depend on interfacial tension, wettability, and the curvature at the interface. A porous medium consists of a network of connected pores, and the medium's heterogeneity and connectivity restrict the fluid's displacement. The ratio of the viscosity of the involved fluids can lead to the formation of viscous fingers. Viscous fingers are instabilities that result in the growth of finger-like structures that form during the displacement of one fluid by another. To better understand the physics of these instabilities in porous media and its applications, we study the effect of medium heterogeneity on flow through experimental research. We do this by designing an asymmetric microfluidic device with a specific geometrical structure and tuning the viscous pressure, wettability of the medium, and capillary pressure within the medium. We horizontally displace air using water, record the behavior of finger growth in the forward direction (which we refer to as the base orientation), and compare it to the displacement in the opposite direction (which we refer to as the apex orientation). We hypothesize that fluid finger growth will be favored in the opposite direction while a more uniform front will occur in the forward direction.

1.1 Microfluidics and Porous Media

Fluid dynamics can describe fluid behavior at large scales using well-established models by assuming that fluids are a continuous medium [2]. However, when dealing with fluid behavior at microscales, these models may become limited or break down as size continues to decrease.

This emerges as a result of the change in factors that dominate the system's behavior. At larger scales inertial forces dominate, leading to the development of phenomena such as turbulent flows. In contrast, viscosity, capillary effects, Brownian motion, van der Waals forces, and interfacial tension are the dominating factors when dealing with microscale fluid behavior. At these small scales, the fluid's behavior depends much more heavily on intermolecular interactions [3-4].

The goal of microfluidics is to study fluids and their physics at these smaller scales. As opposed to general fluid behavior at macroscales being much more intuitive, the microscale behavior of fluids introduces a new level of complexity that goes against human intuition. Various techniques are employed to analyze this microfluidic behavior; one of the most common approaches is using microfluidic chip devices. Microfluidic devices can be fabricated using soft lithography, micro-molding, 3D printing, and micro-machining techniques. These devices are often called "lab-on-chips" and find applications across several disciplines, ranging from biomedical research to oil microfluidics, which mixes geoscience, chemical engineering, and materials science [5-6].

Within the realm of microfluidics lies the study of porous media. Porous media refers to materials with sponge-like qualities at the microscale, featuring networks of interconnected pores. Fluid behavior inside this network is influenced by intrinsic fluid properties such as the viscosity of the fluid, its surface tension, and the contact angle it forms with the surrounding surface. At the same time, the porous medium itself possesses characteristics that can impact the invasion of a fluid, including permeability, porosity, and inter-pore distances, which can redirect or impede an invading fluid's flow. Understanding these properties and how they link with one another is crucial in understanding filtration processes, biological tissues such as bones and lungs, and comprehending transport phenomena within porous media. To understand these elements,

researchers have created simulations and taken experimental measurements of models that replicate these environments [7-9]. There have been suggestions to use these properties of porous media to help in controlling flow by altering the geometry of its structure or by adjusting the contact angle [10-14].

2.0 Theory

2.1 Flow Dynamics in Porous Media

While several factors impact whether a fluid invades a pore in a porous medium, two key factors that dictate fluid flow are the permeability and porosity of the medium, which are both intrinsic to the medium. Permeability represents how easily fluids flow throughout a medium; materials with high permeability are more likely to allow flow, while the porosity of a medium represents how much of the total volume is occupied by empty space. Of course, there are also properties determined by the invading fluid that will alter the characteristics of flow. One of these properties is the fluid's dynamic viscosity, which relates the viscous stresses of the fluid to its strain rate.

Darcy's Law, shown in equation (1), describes a simplified relationship between the volumetric flow rate Q and the pressure drop across two points, represented by Δp, along the flow path of the fluid over a given distance and cross-sectional area in the medium denoted by L and A respectively, through porous media for single-phase flow.

$$Q = -\frac{kA}{\mu L} \Delta p \qquad\qquad \text{Eq. (1)}$$

Here k and μ are the permeability of the medium and dynamic viscosity of the invading fluid, respectively.

Equation (2) shows the hydrostatic pressure equation which describes the change in pressure exerted by a fluid at rest due to gravity. By replacing the pressure drop in equation (1) with the relation for static fluid pressure shown in equation (2), we achieve equation (3):

$$\Delta p = \rho g \Delta h \qquad \qquad \text{Eq. (2)}$$

$$Q = -\frac{kAg}{vL}\Delta h \qquad \qquad \text{Eq. (3)}$$

where ρ is the density of the fluid, g is the acceleration due to gravity, and Δh is the height of the fluid. In equation (3), the dynamic viscosity is replaced by the kinematic viscosity v, which is the ratio of dynamic viscosity to density. Darcy's Law shows that the volumetric flow will differ for different materials. However, the volumetric flow will also differ for the same materials when the direction of flow changes.

2.2 Capillary Pressure

Concepts of flow in porous media can be combined with some asymmetry in the structure to control the flow. Earlier simulations hint that it is possible to achieve a directional-dependent two-phase flow [15]. These 2D simulations incorporate a matrix of triangular-shaped pillars into a porous medium. The findings from this research suggest that as a consequence of incorporating asymmetric porous structures, there exists a natural valve in a pressure regime at which fluids are allowed to flow when the flow is aimed in the opposite direction that the triangles' apex points to,

and fluid flow is impeded when traveling along the direction the triangles' points to. We call these two orientations the **base orientation** and the **apex orientation**, as seen in Figure 1. This follows the logic that in the base orientation, the meniscus of the invading fluid comes into contact with the base of these triangular pillars first. In contrast, in the apex orientation, the meniscus comes into contact with the apex of the pillars first.
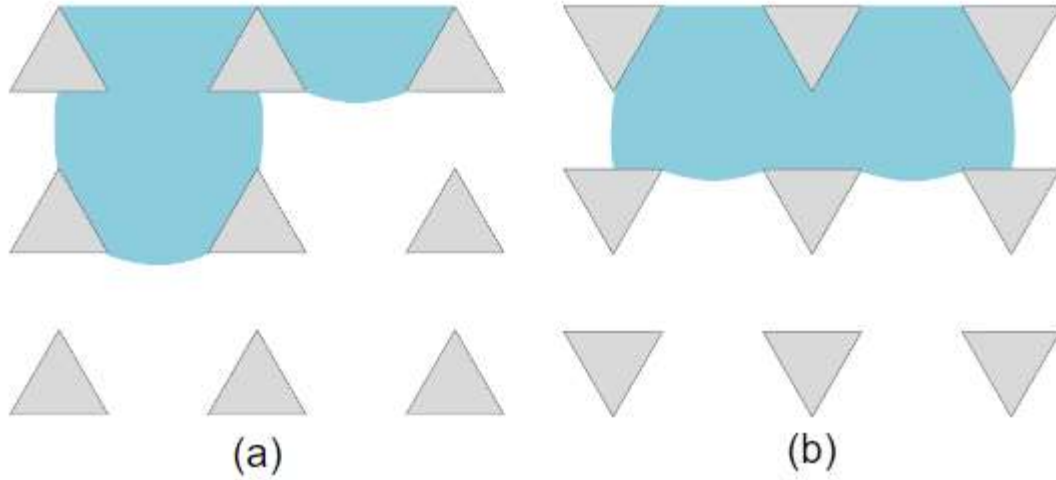
Figure 1 – Difference between the apex (a) and base (b) orientations. Water flows from the top of the medium down, displacing the resident air.

The capillary pressure that must be overcome to percolate through a single pore with a square channel such as shown in Figure 1 can be calculated with equation (4), known as the Young-Laplace equation:

$$p_c = \gamma\left[\frac{\cos\theta_t + \cos\theta_b}{d} + \frac{\cos\theta_l + \cos\theta_r}{w}\right] \qquad \text{Eq. (4)}$$

where p_c is the capillary pressure, γ is the surface tension of the liquid in the microchannel, d, and w are the channel height and width, respectively, and $\theta_t, \theta_b, \theta_l, \theta_r$ are the top, bottom, left, and right contact angles of liquid with the corresponding four microchannel walls. The Young-Laplace

equation relates the pressure difference at the interface between two fluids due to the shape of the surrounding surface and walls.

In our experiments, we can design and plan for the channel dimensions. We choose the invading fluid to be water, as we can use the known value for its surface tension and viscosity. The interfacial tension, also known as surface tension, of water in air is 72 mN/m, and the viscosity ratio of water to air is 1001.6 µPa·s to 18.1 µPa·s. We approximate all four angles to be equal, which leads to equation (5):

$$p_c = 2\gamma \cos \theta \left[\frac{1}{d} + \frac{1}{w}\right] \qquad \text{Eq. (5)}$$

By subtracting the capillary pressure from the hydrostatic pressure when the interface between the two fluids is at equilibrium, we find the pressure difference across the interface, given by equation (6):

$$\Delta p = \rho g h - 2\gamma \cos \theta \left[\frac{1}{d} + \frac{1}{w}\right] \qquad \text{Eq. (6)}$$

Using equation (6), we can estimate the hydrostatic pressure required to percolate through the medium. Then, we can compare the flow rate and percolation depth of the two orientations at specific pressure gradients to find if there is a directional percolation due to asymmetry. We hypothesize, following the simulations mentioned, that there will be a low-pressure regime where both orientations impede flow; as the pressure increases, there will be a regime in which fluid only flows in one direction, and finally, there will be flow in both directions at higher applied pressures.

3.0 Experimental Design and Methods

3.1 Overview

Fabrication of microfluidic devices has become a lot more accessible over the past few decades. As of the late 1990s, researchers have started using polydimethylsiloxane (PDMS), a silicone-based polymer that is well-known by scientists and engineers due to its ease of use and cost-effectiveness for microfluidic experiments when compared to previous methods of creating devices [16-18]. In addition to PDMS, with 3D printing technology, it is possible to design microfluidic molds and fabricate microfluidic devices out of PDMS at much larger scales.

3.2 Mold Development and Design

The first and one of the most significant steps in the experimental process is designing the microfluidic device used in experiments. Using concepts of capillary displacement in porous media, we draft a device design plan that we believe can achieve a directional percolation. These devices are fabricated using microfluidic molds designed using AutoCAD and then printed in resin using digital light processing. Once the final draft of the microfluidic device is finished, it is replicated as a 2D outline using AutoCAD software. We use a CADworks3D H-Series 3D printer that prints at a 30 x 30 x 5 (x y z) μm resolution. To ensure that the AutoCAD design adheres to the resolution of our printer, we adjust AutoCAD's settings to match the printer's resolution before creating the 2D outline. Devices are designed starting with a draft of the porous medium. We complete the device using the former as a base.

The porous medium in our experiments consists of a matrix of evenly spaced triangular-shaped pillars. This shape is chosen due to its asymmetry. Compared to other simple shapes, when

rotated by 180 degrees, triangles exhibit more asymmetrical properties. The size and dimensions of these triangular pillars are based on adjusting the capillary pressure necessary to allow percolation within the medium. While larger pores would allow for a fluid invasion to occur at lower pressures, we expect them to increase the sensitivity of our experiments as there will be less resistance to flow. We apply pressures no larger than 1500 Pa, so we attempt to design the medium in a way that causes the pressure boundary at which percolation begins to occur to lie within the upper limits, allowing us to take full advantage of the applied pressure window. This is done by controlling the spacing between the triangular pillars in the medium.

By reducing the size of the triangular pillars and the distance between them, percolation will occur at higher pressures, decreasing our experiment's sensitivity. Inversely, the triangular pillars must be large enough to retain their triangular shape when compared to the meniscus of the invading fluid. If the triangular pillars are too small, the meniscus of the invading fluid may treat them as point-shaped obstacles rather than as triangular barriers when they meet. Additionally, having larger pillars will help the printed molds avoid pixelation caused by our printer's resolution as shown in Figure 2.

The final and perhaps most important part of the design is the difference between the distances between the apex of the triangular pillars and their base. To maximize the possibility of observing a directional percolation effect, we place the triangular pillars in a pattern that causes the distance between their apexes to be more than five times larger than the distance between their bases. This relationship can also be changed according to triangle size, with larger triangular pillars yielding a larger difference between spacings. Determining a proper size for the triangles is difficult due to its many effects on the experiment.
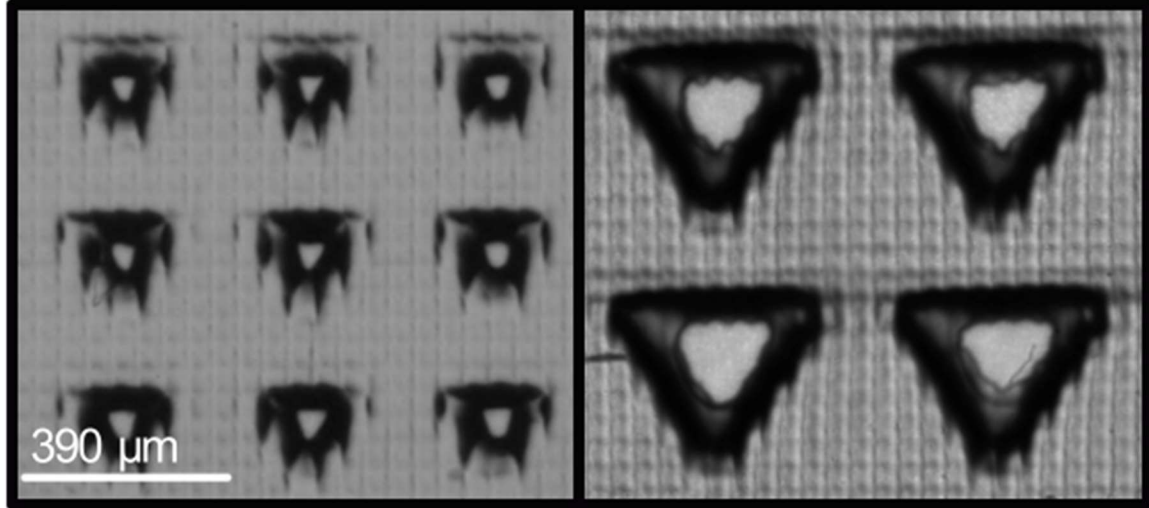
(a) 60 µm side length pillars (b) 390 µm side length pillars

Figure 2 - A comparison of equilateral triangular pillars with a 60 µm and 390 µm side length after having been made with their respective molds. (a) shows the smaller pillars taking on a more point-like shape due to pixelation after a device is fabricated. The spacing between each smaller pillar's apex is three times larger than between their bases (300 µm compared to 90 µm). Meanwhile, (b) shows that the large pillars can retain their triangular properties after fabrication. The spacing difference between the apex and base of one pillar and the next is much larger than the one shown in the 60 µm side length case (480 µm and 90 µm, respectively).

When pillar size is determined, we position the triangular pillars so that the minimum distance between them along the horizontal direction is approximately the same as the minimum distance in the vertical direction, differing slightly only due to resolution limitations. The latter is done to prevent a bias regarding horizontal or vertical invasion based explicitly on throat size (which refers to the space between two pores or channels). Throat size dimensions can influence fluid flow, filtration, and other processes occurring within the microfluidic system. The dimensions of a pore can be seen in Figure 3.

The final design of the porous medium consists of a network of 34 x 42 triangular pillars. A benefit of designing a larger medium is that it causes a reduction in the sensitivity of our experiments, similar to a medium with smaller pore sizes. Individual perturbations will have less

impact in a larger medium due to the more extensive network acting as a whole. This gives more flexibility regarding instabilities and Haines Jumps [19], where the invading fluid flows fast enough to where its momentum and inertia affect how it invades the next pore. Since there is a larger length that the fluid can cover before exiting the medium, these occurrences will matter less.
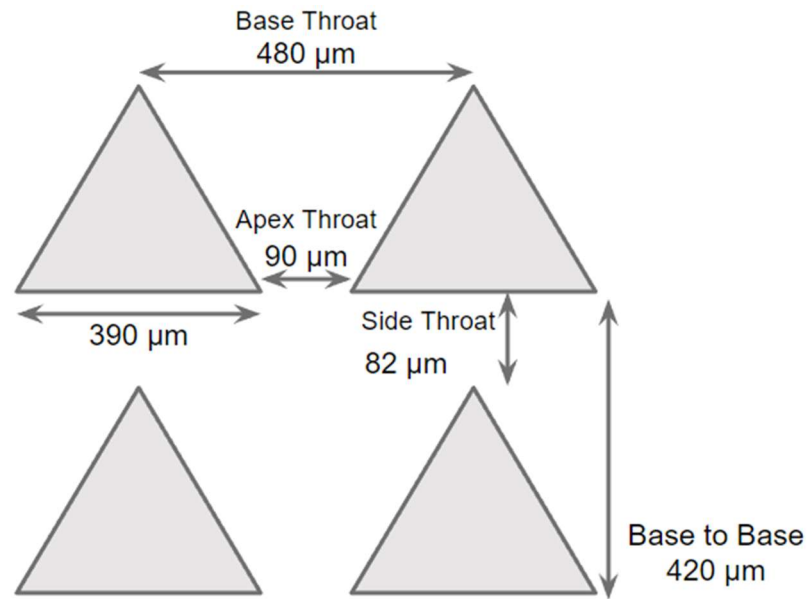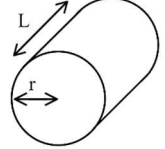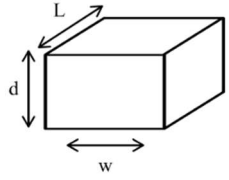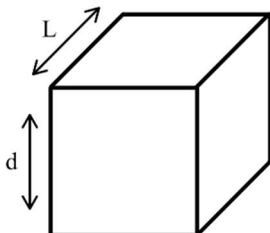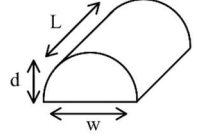
Figure 3 - A diagram showing the dimensions of the 2D triangles inside the porous medium design before they are extrapolated. The length of each pore's side and apex throat are designed to be as similar as possible. The base throat is 5.33 times larger than the apex throat. With the triangles being equilateral, they create a 60° angle with the horizontal. This setup is extrapolated to a matrix of 34 rows and 42 columns.

The next part of the AutoCAD design process involves creating the border of the microfluidic device that will surround the porous medium. This involves adding an inlet, outlet, and channels connecting them to the porous medium. The inlet and outlet are large regions within the microfluidic device. These are made to mark the location that will be pierced to allow for the insertion of microfluidic tubing into the finalized device. The inlet refers to the region from which

the fluid enters, while the outlet refers to the area from which it exits. The channels connect these two regions to the porous media. They are made in a long snake-like shape to achieve a stable-instability free flow, which is the ideal situation for our experiments, as it will assist in yielding higher quality data when aiming to obtain a threshold of pressures in which a directional percolation effect occurs.

To ensure that flow instabilities at the inlets do not abruptly perturb the fluid flow within the porous medium, we calculate the width and length of inlet channels. Using the Hagen-Poiseuille equations shown in Table 1, we design the channels to have enough resistance that the invading fluid is flowing at a slow enough flow rate that when it reaches the porous boundary, it comes to a stop and makes contact along the whole boundary line before it begins percolating through any pores. The resistance of a channel depends on several things, such as the geometry of the channels, the surface of the material they are made of, and the viscosity of the fluid flowing across the surface, to name a few. During this step, we need to plan for the design to allow for an even flow distribution into the medium; this is done by creating evenly spaced channels that branch off the snake. In the design, each channel is split into two separate branches, with three generations of split branches. This results in eight 450 μm branches spaced roughly 2.38 mm apart, from which a fluid can enter or exit from the porous media.

Table 1 - Channel Resistance for Common Geometries

Geometry	Channel Resistance	Figure
Circular	$R = \dfrac{8}{\pi}\eta L \dfrac{1}{r^4}$	
Rectangular	$R \approx \dfrac{12}{1 - 0.63\dfrac{d}{w}}\eta L \dfrac{1}{d^3 w}$	
Square	$R = 28.4\eta L \dfrac{1}{d^4}$	
Parabolic	$R = \dfrac{105}{4}\eta L \dfrac{1}{d^3 w}$	

We specifically design microfluidic devices to be bilaterally symmetrical except for the medium. As our experiments are directionally dependent, making the device design bilaterally symmetrical allows us to use the design for both the apex and base orientations. With the branch's

finalized design, we encapsulate the porous medium, as shown in Figure 4. We make sure to leave ample room for the fluid to disperse evenly before coming into contact with the medium.
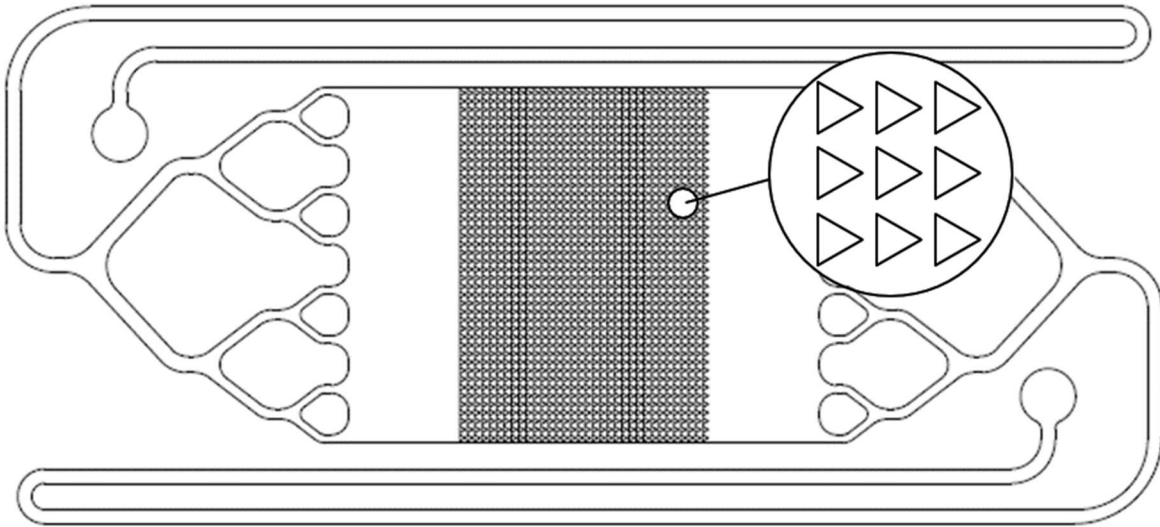
Figure 4 - The completed 2D AutoCAD schematic before extrapolation has been applied. Notice the medium is a tightly packed matrix of triangles.

Once the 2D outline of the design is done, we must turn it into a 3D structure for printing. To achieve a parabolic flow profile as seen in Figure 5, we design the height of a microfluidic device to be equal to the minimum throat thickness, which happens to be 90 μm. This is done by extrapolating the negatively spaced design to a 90 μm height once completed, creating the 3D schematic. This gives a square-shaped channel instead of a rectangular one, allowing us to achieve parabolic flow more readily. However, it's important to note that there will still be a rectangular channel between the apexes of the triangular pillars.

Parabolic Flow Side Profile
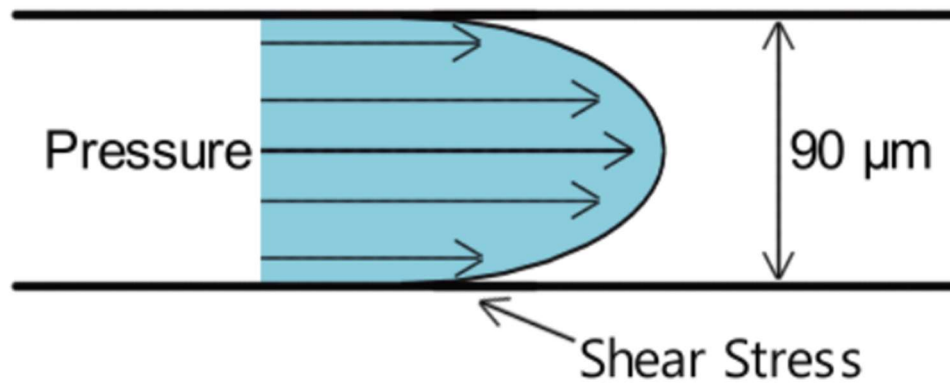
Figure 5 - Schematic of parabolic flow through a microchannel. The flow of the front is symmetrical across the center of the parabolic profile. This shape is due to the shear stress caused by the relative motion between the invading fluid and the microchannel.

Keeping in mind that we are printing a mold using a 3D printer, we add a molding base after extrapolating the negative parts of the device. Thankfully, AutoCAD does a great job at extrapolation with the "press pull" tool. This tool can be used to extrude 2D objects into 3D shapes easily. By having the user select an enclosed 2D shape, AutoCAD identifies the shape and detects the boundaries within the closed area. Then, the user can determine what height to extend the design to. After extruding the finished design to the previously mentioned 90 μm height, we surround it with a base and an elevated boundary as seen in Figure 6. The PDMS device's thickness influences its hydrophobic recovery time, so we design all of the molds to be 7 cm tall. This also applies to molds used to create the bottom part of the microfluidic devices, which only include the base and elevated boundary, not the device's design.
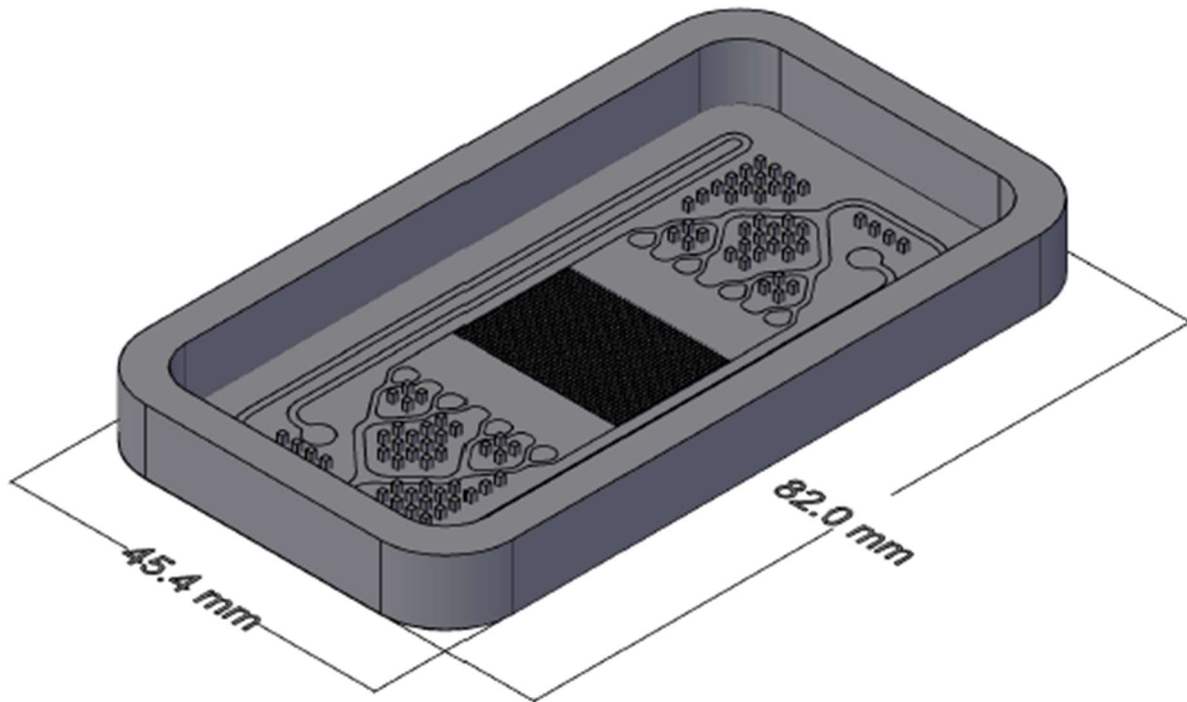
Figure 6 - The completed 3D AutoCAD schematic after extrapolation has been applied. The additional cubes planted on the base of the mold assist with pulling out the device once the mold is used. Additionally, they help adjust the devices when performing the bonding process.

3.3 Mold Printing

After finishing the mold's completed design in AutoCAD, we export it as an .stl file and use the software provided by CADworks3D to connect it to our microfluidic printer. This program allows us to adjust the coordinates and rotation of the mold on the printer's build plate; it also shows a preview of what the mold will look like when it is done printing. Once we adjust the 3D schematic's placement on the build plate, we convert it into a .3dp file and load it into the printer to start the digital light processing step.

Digital light processing, as shown in Figure 7, is performed after lowering the build plate into a resin vat. Once the build plate is in the resin, a digital light projector with a wavelength of

385 nm cures the resin onto the stage plate according to the .3dp file. As mentioned previously, the printer has a 30 μm micron resolution in the length and width dimensions, a five μm resolution in height, and prints layer by layer onto the plate. This step usually takes one to three hours, depending on the design's height. Once printed, the mold is still covered in uncured resin, so it must then be vigorously cleaned to remove the uncured resin and any cured granules that remain on the surface of the mold. This involves soaking the mold in an isopropenyl alcohol (isopropyl alcohol) bath for ten minutes, drying it off with pressurized air, and soaking it in a new, clean isopropenyl alcohol bath for another ten minutes before drying again. It is then cured once more with UV light for 50 minutes.
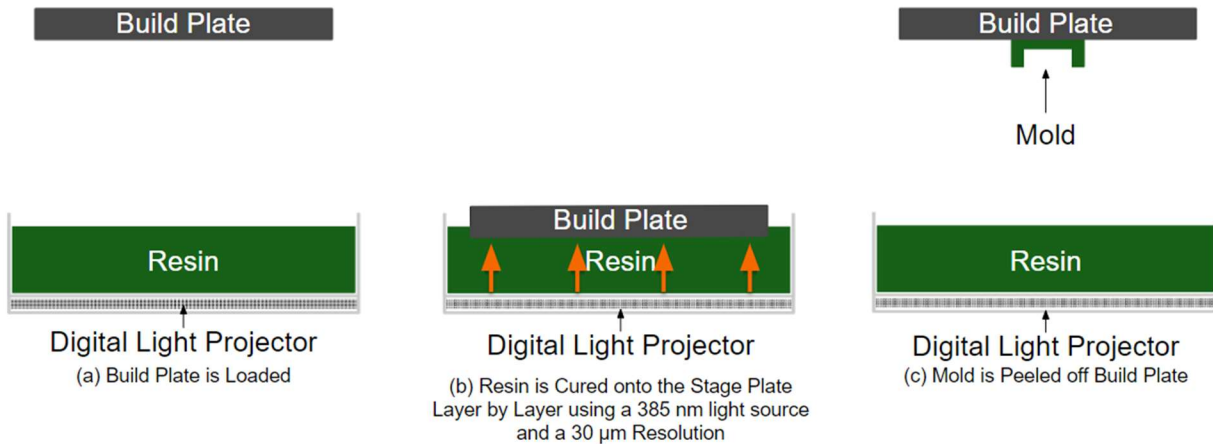
Figure 7 - Representation of the digital light processing used by the 3D printer to create a mold out of resin. The mold is cured layer by layer during step (b) and released during step (c).

3.4 Microfluidic Device Fabrication

The physical devices are created by curing PDMS (polydimethylsiloxane) into molds created in the previous steps. We use Sylgard 184 as our commercially available PDMS, which is manufactured by Electron Microscopy Sciences, and a 10:1 cross-linker agent is included when purchasing the product. After filling the mold with PDMS, it is placed in a vacuum desiccator to

degas the PDMS, which removes any air bubbles that form while pouring. It is allowed to completely cure, which takes approximately 24 hours. Then, we peel the PDMS out of the mold using a razor to cut into the sides and pull it out using a pair of tweezers. Once we have the cured slab of PDMS, we need to clean and prepare it for the bonding process. Cleaning involves rinsing it with isopropenyl alcohol and punching holes into it to create the inlet and outlet; it is then submerged in isopropenyl alcohol and sonicated for 15–20 minutes. The sonicator uses high-frequency sound waves to disperse any particles attached to the PDMS's surface. Once the time has passed, we rinse it with isopropenyl alcohol again and place it in an oven at 60 °C to bake until dry. This is done for both PDMS parts of the device, the base, and the patterned pieces.

Once the device is dry, we move to the plasma bonding process. This process is done by plasma treating the surfaces of both device layers, which chemically activates both surfaces. This is done using a low-pressure, non-thermal plasma etching wand. As the plasma comes into contact with the surface, we achieve the formation of silanol (Si-O-H) groups. It is worth noting that plasma treatment causes the surfaces of the devices to become highly hydrophilic, but it recovers its hydrophobicity over time. This is due to the formation of the previously mentioned silanol groups. The introduction of these groups increases the surface energy of PDMS and renders it more hydrophilic. Over time, the silanol groups on the surface of the substrate will degrade, causing the surface to recover its hydrophobicity as shown in Figure 8.
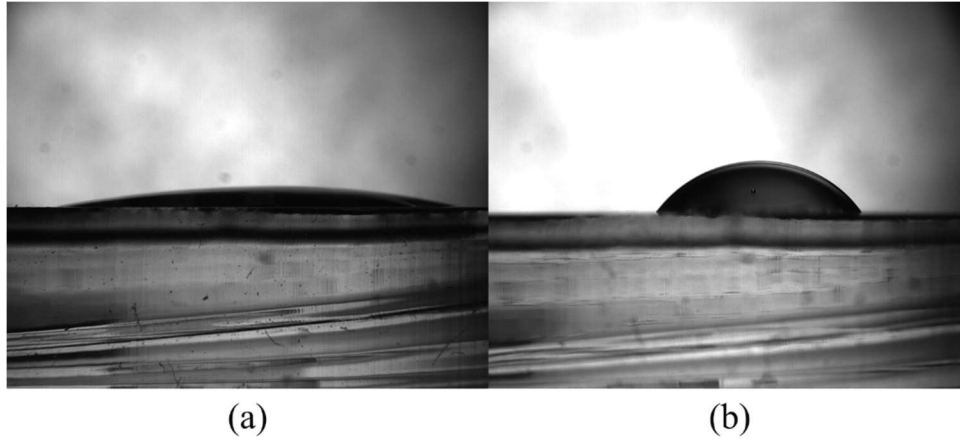
Figure 8 - Comparison of a water droplet on PDMS one hour (a) and three hours after plasma treatment (b). Notice how the droplet in (a) is barely visible compared to the droplet in (b) due to the difference in wettability.

We treat the surface of both parts of the device simultaneously, in parallel, for one minute under a constant stream of dry air. This is to ensure that we get a good bond, as we have observed that not treating the PDMS slabs for a long enough period of time causes a faulty bond, and having a high humidity level causes the water vapor in the air to react with the surface. Inversely, plasma treating the device surfaces for too long will cause bonding to fail [20]. After activation, we immediately bring the two pieces into contact and apply pressure. This causes the silanol groups on both surfaces to chemically bond with one another as shown in Figure 9. To ensure the two pieces of the device are correctly bonded, we attempt to peel the device apart; if successful, we restart the process, beginning with a new PDMS pour.
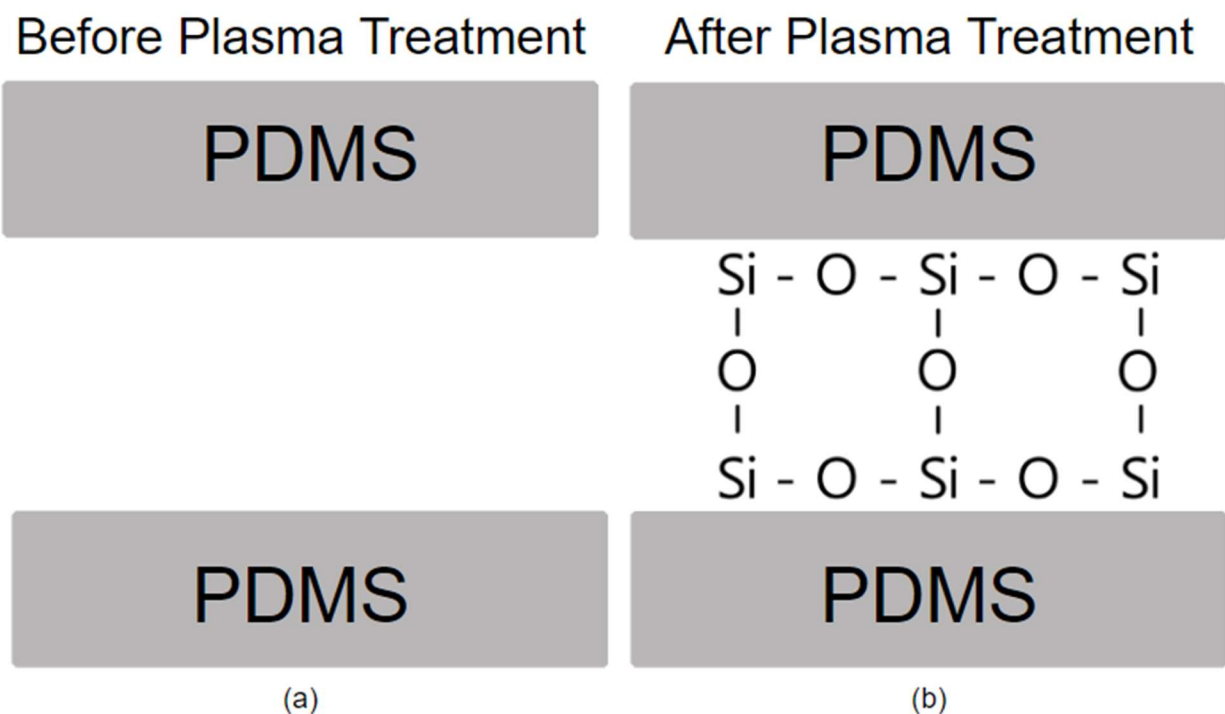
Figure 9 - Chemical bonding between PDMS after plasma surface activation and contact. Silanol groups form on both surfaces, which then react with each other when brought together. This can also be done with PDMS and a glass slide.

It is crucial to maintain a clean environment during this step. If hairs, dust, particles, or contaminants land on the surface as it is being treated, it can result in a faulty bond. To keep the device clean while exposed and remove any contaminants on the surface before treatment, we apply scotch tape onto the surface and peel it off before plasma treatment.

Once bonded, we bake the devices in an oven at 60 °C overnight. Additionally, since we can't measure the contact angle directly inside the device, we create a separate control slab and apply the same process without bonding it to another. We then measure the slab's contact angle with distilled water and use that as a reference for the contact angle inside the finished microfluidic device.

3.5 Wettability Modification

The contact angle between of water on the device walls is extremely important for this experiment since it impacts the capillary pressure. We estimate the hydrostatic pressure required for water to percolate through the medium using equation (6). Therefore, it's crucial for us to properly determine the contact angle of the surfaces. To do this, we've created a setup consisting of a backlit elevated platform using a collimated LED. To make contact angle measurements, we use a Thor camera with Thorcam software to take a side-view image of 20 µL droplets that are dropped onto a PDMS slab as .tiff files (Figure 10).
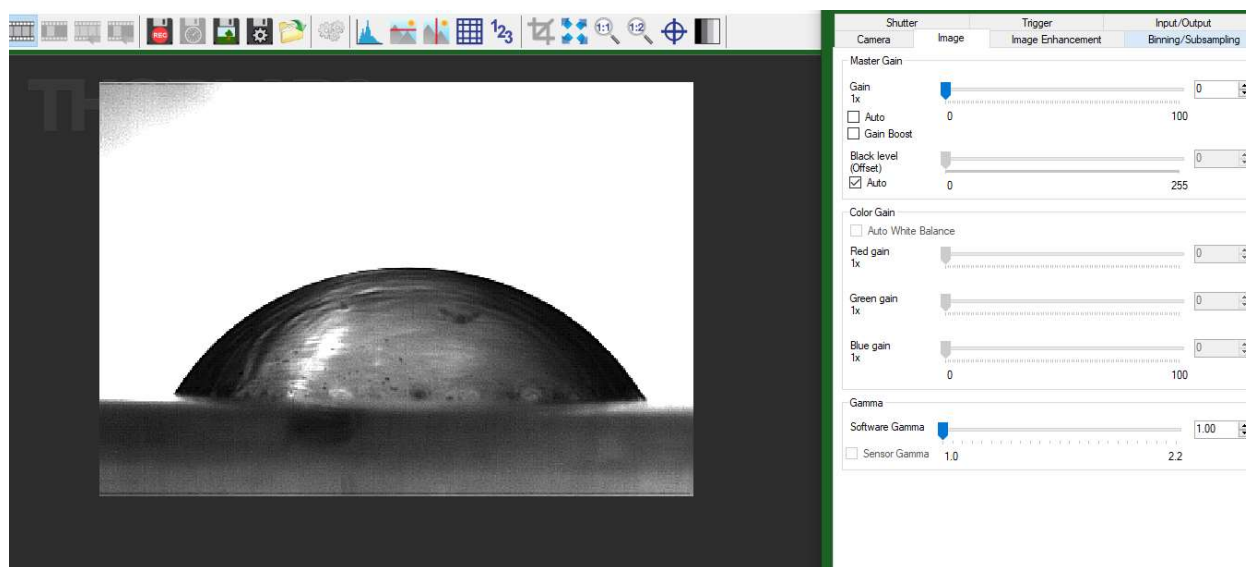
Figure 10 - Thorcam software interface used to image a 20 µL droplet. The settings on the right-hand side of the figure allow for image quality enhancement by adjusting the gain and gamma values, including others.

Droplet contact angle measurements are taken after applying specific silanes to the slab's surface immediately after plasma treatment and as a function of time since plasma treating the slab's surface. We previously mentioned that plasma treatment causes the activated surface of the treated device to become hydrophilic. Over time, the surface will recover its hydrophobic properties.

We exercise two different methods of modifying the surface with silane treatments using 1H,1H,2H,2H-Perfluorodecyltrichlorosilane, 96% (FTCS), n-Decyltrichlorosilane, 97% (which we will reference as ND), and hexamethyldisilazane (HMDS). For FTCS and ND, we create solutions in both hydrofluoroether (HFE) and ethanol at concentrations of 1, 5, and 10%. We then place each of these solutions under a vacuum in a desiccator, with plasma-treated slabs of PDMS and glass slides, allowing the solution to fully dissipate throughout the desiccator chamber in a manner similar to chemical vapor deposition. We do this multiple times for each solution in an attempt to coat the surfaces of our device by deposition (Figure 11). Additionally, this is also done for pure HMDS.

As another method of modifying the contact angle, we also pour the different solutions and pure FTCS and ND onto clean, freshly plasma-treated glass slides and PDMS slabs. Then, we take contact angle measurements using the previously mentioned process.

These two methods coat the two different surfaces in a silane layer, aiming to achieve the same contact angle for both pieces of the microfluidic device. As the plasma treatment exposes silanol and hydroxyl groups, it is imperative to expose the surface to silane as fast as possible, as the silane attaches much better to these molecules.
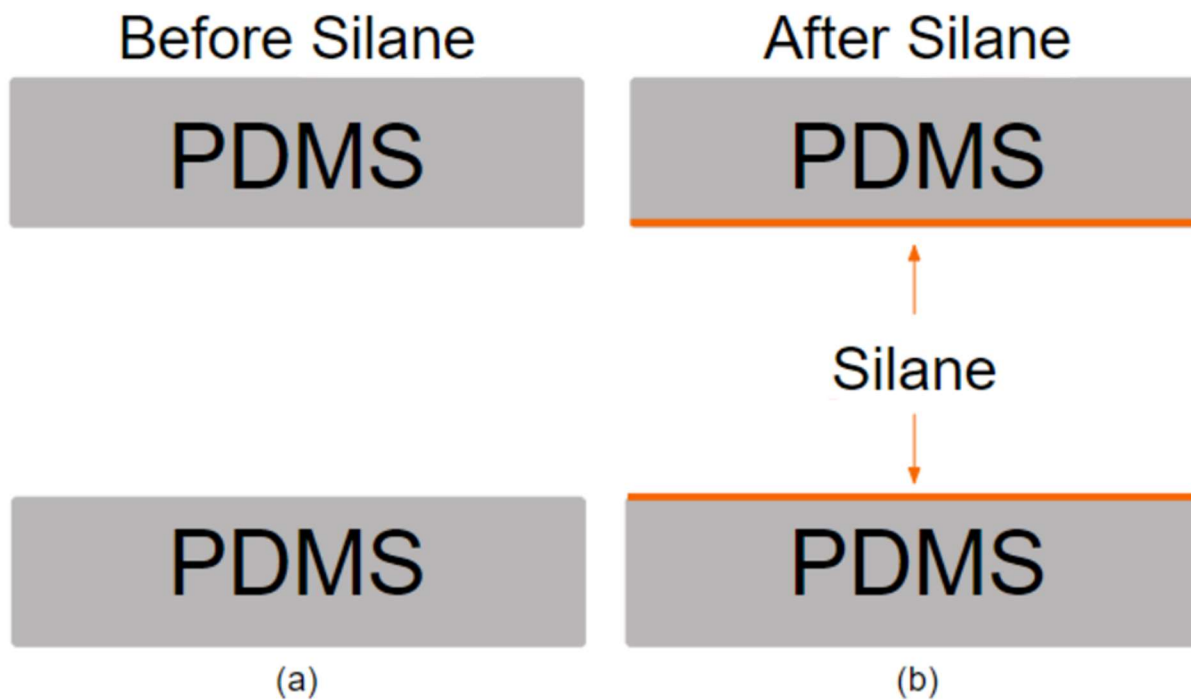
Figure 11 - Schematic of an ideal microfluidic device before (a) and after (b) silane treatment. Notice the small layer of silane covering the PDMS device's whole surface in (b). The PDMS can be replaced with glass for silane treatment.

3.6 Device Preparation and Purging

Before beginning an experiment, we prepare the device to ensure minimal moisture is stuck inside. PDMS is a porous material and tends to absorb moisture over time. To minimize issues that can occur due to this absorption, the devices are placed in a desiccator under vacuum for five minutes before performing experiments. With a special attachment on the desiccator, microfluidic tubing is fed into the inlet or outlet of the device. This allows us to remove the air in the desiccator while simultaneously having the air pass through the microfluidic device. This setup aids in eliminating gas and moisture from the PDMS before experiments.

After experiments, we flush all channels and pores in the device with distilled water to clean it. Then, we flush out as much water as possible from the device before placing it in the oven

overnight. Combining this step with the device preparation enables us to keep similar conditions between different experiments in the device's environment.

3.7 Experimental Setup and Measurement Techniques

Our experiments can take up to 24 hours, so we use a Fastec camera with two terabytes of storage and a wide-field Zeiss axio-zoom microscope to visualize and record the flow across the entire medium at once. Since these experiments are done at pressures no larger than 1500 Pa, we use a column filled with distilled water in our setup. This column acts as a hydrostatic source of pressure for our setup, as seen in Figure 12. Since we are interested in seeing how percolation changes at different pressures, we avoid steady-state hydrodynamic flow, where a fluid is subject to a constant flow rate. If we use a constant flow rate, we will always see a percolation through the medium instead of the possibility of invasion being halted halfway through the experiment in a hydrostatic case.

Therefore, we achieve equation (7) by setting the pressure difference in equation (6) equal to zero to find the approximate height needed to match the capillary pressure.

$$\rho g h = 2\gamma \cos\theta \; [\frac{1}{d} + \frac{1}{w}] \qquad\qquad \text{Eq. (7)}$$

To adjust the external applied pressure, we have created our setup using a micrometer to allow for precise changes to height. To record data, we center the device under the camera and illuminate it using a collimated LED, as it will provide us with a beam of light that causes minimal spreading. Since our experiments can last up to 24 hours, we submerge the device in distilled water. PDMS is permeable, and over time, air bubbles will appear in the channels that connect the

inlet and outlet to the medium, interfering with the experiment. While the device is submerged in water, this becomes impossible.
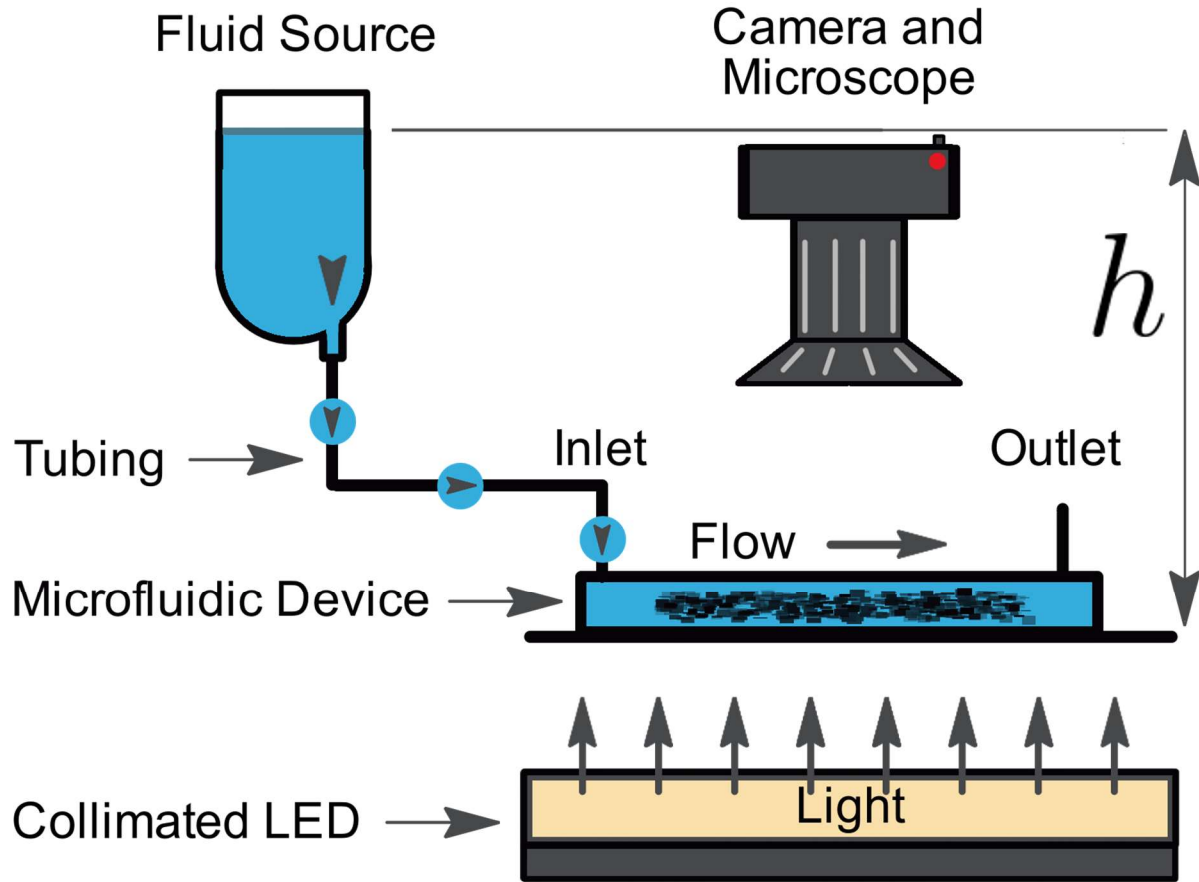
Figure 12 - Schematic of the experimental setup with a pressure adjustment via liquid column and microfluidic device height difference. As the height of the liquid column increases, pressure increases linearly. When adjusting the height, first, we determine the desired pressure for the experiment and adjust the height accordingly.

When preparing for our experiment, after connecting the liquid column to the microfluidic device using 0.863 mm inner diameter wide microfluidic tubing (1.3208 mm outer diameter), we adjust the pressure to allow the fluid to flow slowly through the channel. This ensures that it flows evenly through the split branches once it reaches each generation of branches. We allow the fluid

to flow through the branches and reach the opening before the media; then, we ensure that it comes into contact with the whole porous boundary. Then, we change the pressure to a constant value at which the experiment will be performed and allow the experiment to elapse for up to 24 hours, taking a burst of images of the percolation of the invading fluid every ten seconds.

The pressure values we use are based on a pressure gradient to find the minimum pressure at which fluid begins to percolate through the porous medium. Since we are interested in the pressure boundary at which there is a geometrical percolation effect, we must first determine what pressures to use for our hydrostatic experiments. To do this, we allow the invading fluid (distilled water) to flow through the branches and reach the opening before the media; then, we set the pressure to 400 Pa and allow the fluid to settle. Then, every 15 minutes, we increase the pressure by 100 Pa until the fluid fully percolates through and reaches the other side of the medium. This yields the gradient of pressure to try for our experiment.

When performing experiments, we always begin with the base orientation of the device, as we believe that it should exhibit higher values of pressure at which the fluid percolates. We then repeat the experiment with the opposite (apex) orientation and compare the two. This pairing is done multiple times to collect data across various pressure values.

4.0 Results and Discussion

The outcomes of this study demonstrate that the asymmetry of a porous medium controls first-order instabilities at air-water interfaces, leading to the development of fluid fingers. The contact angle at the interface is an essential factor in determining the capillary pressure. Hence, we start with quantifying the contact angle. This is done by comparing the results of different surface treatment methods and identifying which yields the highest contact angle. Then, once this method is found, we perform our experiments in a hydrophobic environment at pressures between 800 and 1000 Pa.

4.1 Contact Angle Characterization

PDMS surface treatment is done using different silanes or by allowing the PDMS to recover its hydrophobicity naturally over time. The goal is to find a treatment that yields a high yet consistent contact angle above 100°. A lower contact angle will result in a lower capillary pressure, causing our experiment to become more sensitive, while an inconsistent contact angle will cause overall inconsistent results in our data.

4.1.1 Chemical Treatment with Silane

While promising at first, we find that chemically modifying the surface of the devices with silane, even right after plasma treatment, proves more difficult than expected. In cases where we use a solution of silane mixed with ethanol or HFE and spread it on the surface, we find that the contact angle is way too low for our experiments (less than 90°) and lands in the hydrophilic regime (see Figure 13). When pure silane is used, the contact angle is still low compared to our goal but

measures much higher than when the silane is applied while mixed in a solution. Table 2 contains the summarized results of the contact angle based on silane treatment.

To treat the bonded microfluidic devices with silane, we must flow the silane evenly throughout the whole microfluidic device, from inlet to outlet. This involves filling every single pore and every branch within the device to achieve a uniform coat. This doesn't prove easy with the presence of air bubbles. There are also cases where the silane leaves residue throughout the medium during treatment, even after purging with isopropenyl alcohol or ethanol, which causes potential clogging and contamination.

On the other hand, when we treat the surface of the samples with the vacuum-enhanced vapor deposition method, we observe no change in contact angle, even after the solution fully evaporates and dissipates.

Table 2 - Comparison of Contact Angles Based on Different Silane Surface Treatment Methods

Chemical Name	Chemical Formula	Concentration	Method	Range of Contact Angles
n-Decyltrichlorosilane, 97% (ND)	C10H21Cl3Si	10%	Physical Coating	43°-51°
		Pure	Vapor Deposition	Below 40°
			Physical Coating	83°-97°
1H,1H,2H,2H-Perfluoro-decyltrichlorosilane, 96% (FTCS)	C10H4Cl3F17Si	Pure	Vapor Deposition	Below 40°
			Physical Coating	98°-105°
Hexamethyldisilazane (HMDS)	(CH3)3SiNHSi(CH3)3	Pure	Vapor Deposition	Below 40°

Figure 13 - Glass sample treated with a 10% n-Decyltrichlorosilane, 97% solution in ethanol. The contact angle between the droplet of water and the glass slide is measured at 49°

4.1.2 Hydrophobic Recovery of Sylgard 184 After Plasma Treatment

As an alternative approach to modifying the surface with silane, we can allow the PDMS to rest and recover its hydrophobicity naturally, as seen in Figure 14. This method takes longer, however, we prefer this method due to its predictability and cleanliness.
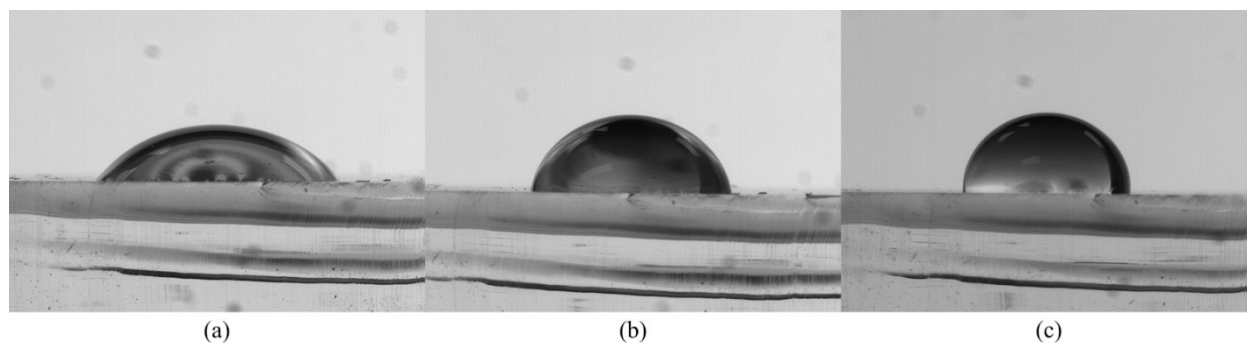

Figure 14 - Image comparison of the hydrophobic recovery over time of a bare slab of PDMS that has been plasma-treated. (a) shows a 50° contact angle after just 6 hours, (b) a 78° contact angle after two days, and (c) a 91° contact angle after seven days.

4.2 Contact Angle Analysis

Contact angle analysis was done using ImageJ, a public-domain software for processing and analyzing images [21]. Additionally, we used a model called "Low Bond Axisymmetric Drop Shape Analysis" to determine the contact angle. The Drop Shape Analysis model is based on fitting the Young-Laplace equation to the image data [22]. The free software model is part of an online Java plug-in for ImageJ.

We manually adjust different parameters to fit a green bordering outline onto a 20 µL droplet using the Drop Shape Analysis model. Once close, we can optimize the outline parameters using automatic tools built into the model. This model's output will yield the droplet's approximate contact angle, as seen in Figure 15.

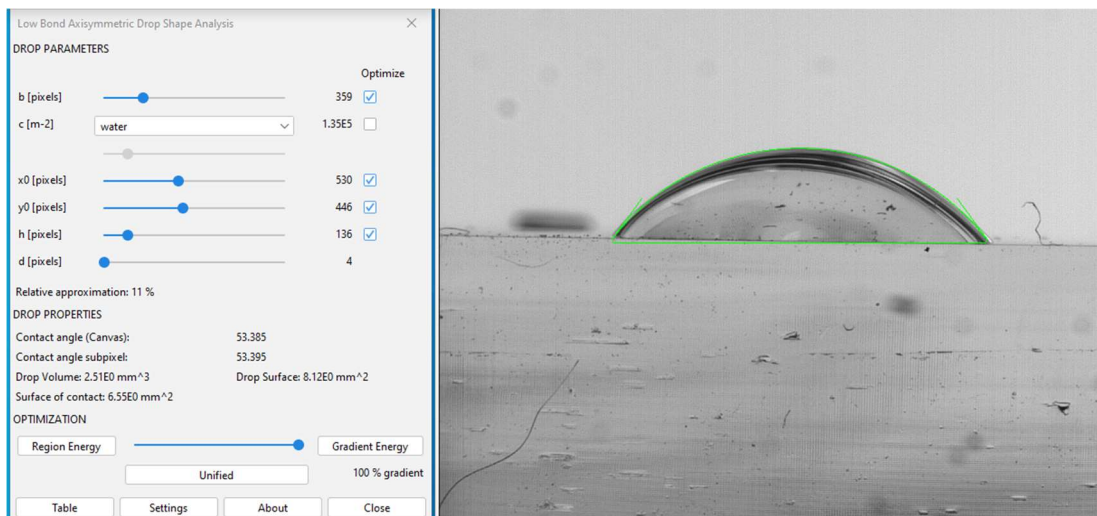Figure 15 - Example of a droplet being analyzed using the Drop Shape Analysis model and ImageJ. The droplet shown in the figure was measured six hours after the PDMS slab underwent plasma treatment and is measured to be 53°.

After measuring and collecting multiple droplet data over two weeks, we can plot the data taken as a function of time (Figure 16). Doing so helps us determine an appropriate wait time

before performing experiments to ensure the devices are hydrophobic. We find that with this

method, devices take approximately two weeks to be fully prepared for experiments.
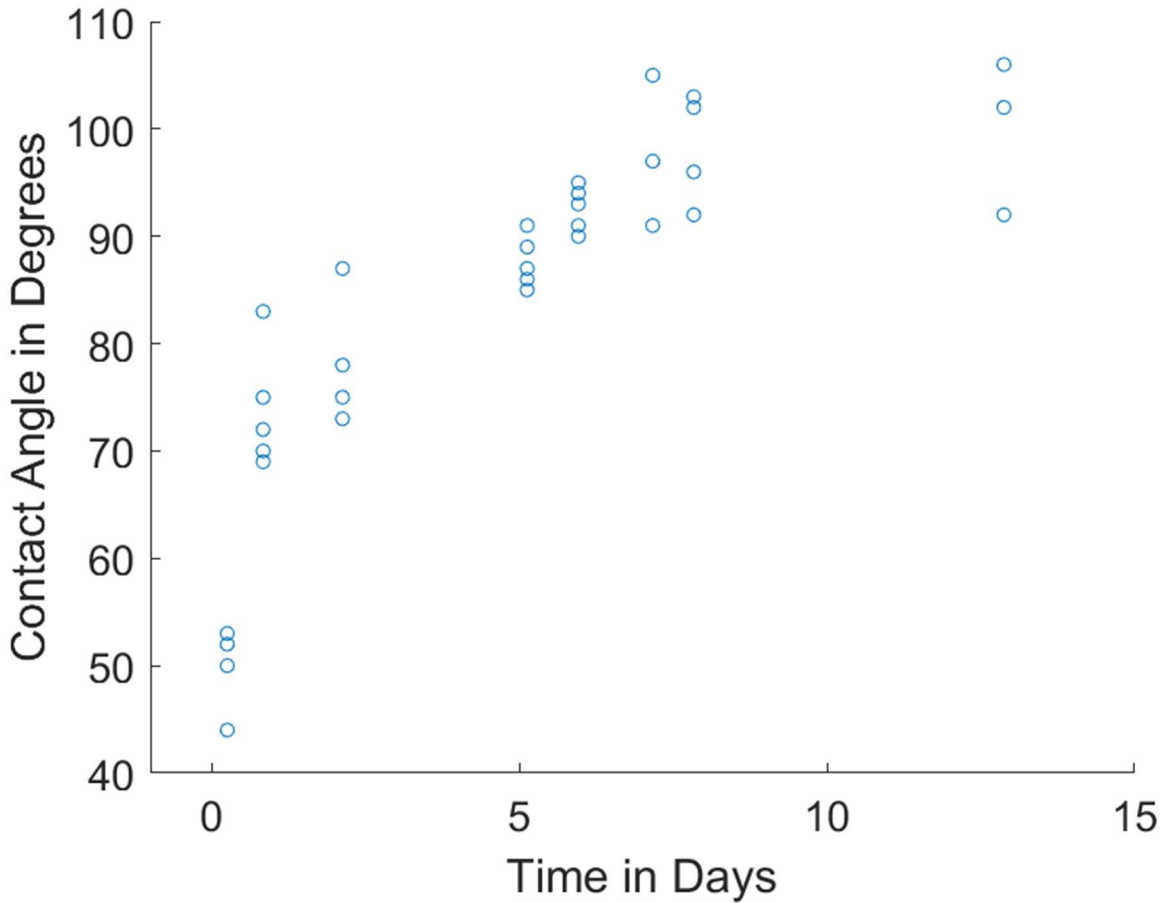
Figure 16 - Hydrophobic recovery of PDMS over time. Between 6 and 24 hours, the contact angle between PDMS and water increases dramatically and continues until two days have passed. At this point, it continues to increase but at a much slower pace. After eight days, the contact angle reaches an entirely hydrophobic regime and remains steady. To ensure devices are hydrophobic, we allot an additional six days of rest before initializing experiments.

4.3 Image Analysis Methods

We record our experimental data in bursts every ten seconds and every ten minutes for experiments over 3 hours. Since we use every frame for data analysis, a ten-second interval allows us to record the events that occur in the medium while keeping our data pool at a moderate size. These images are saved as .tif files, and we use MATLAB image analysis techniques to create an overlay of the experiment. We can extract important information such as the percolation depth, saturated volume, spread, and rising patterns across our experiments using the overlay.

We create two different sets of overlays. The first set, which enables visualization of flow through the medium over time, involves dividing the experiment into five evenly-spaced images, as seen in Figure 17. These images are added on top of each other to show the displacement of the fluid throughout the experiment. This is done by taking the starting image as a base image and subtracting it from each interval image. This is done by converting each image into a matrix that depends on the intensity values of each pixel. Since similar regions between the two images will have almost identical intensity values, the matrix that results from subtracting the two images yields low-intensity values at coordinates where the images are the same and high numerical values at coordinates that are different between the two images. Depending on the intensity difference between the interval and base images, we turn the resulting matrix into a binary image filled with 1s and 0s. This is done by applying a filter to the matrix that turns its values into 1s only if they are above a certain intensity threshold and 0s if below. These 1s and 0s represent regions that have been filled with water and regions that are still unfilled, respectively. However, this usually yields a very noisy binary image depending on the images.

Figure 18 shows the noise reduction, where water is connected by pixels, while the solid structure appears in our images as clusters with fewer pixels. To extract solely the connected

regions of water in these binary images, we remove clusters with small numbers of pixels, an average of smaller than 500 pixels. This results in an apparent separation between the filled (shown in yellow) and unfilled (shown in blue) regions. Notice in Figure 18 (b) that there exist cases where large clusters of noise get through the filtering step. Attempting to remove these causes a loss in the resolution of the filled regions by shrinking the bordering edge backward into itself. For this reason, larger noise clusters are not extracted.

Once the five binary images have been filtered for noise, we can add them together and create an overlay (Figure 19). Since the matrices are filled with 1s and 0s, this overlay will contain higher numerical values in regions where an overlap between the matrices exists. These higher numerical values correspond to the regions invaded by water earlier in the experiment. With the final matrix, we assign time values to each value depending on the length of the experiment, with 5s being the earliest invaded regions and 1s being the last invaded region. Any 0s left in the final matrix represent regions not invaded by water. After assigning time values, we can show an image with a color code, as shown in Figure 20.
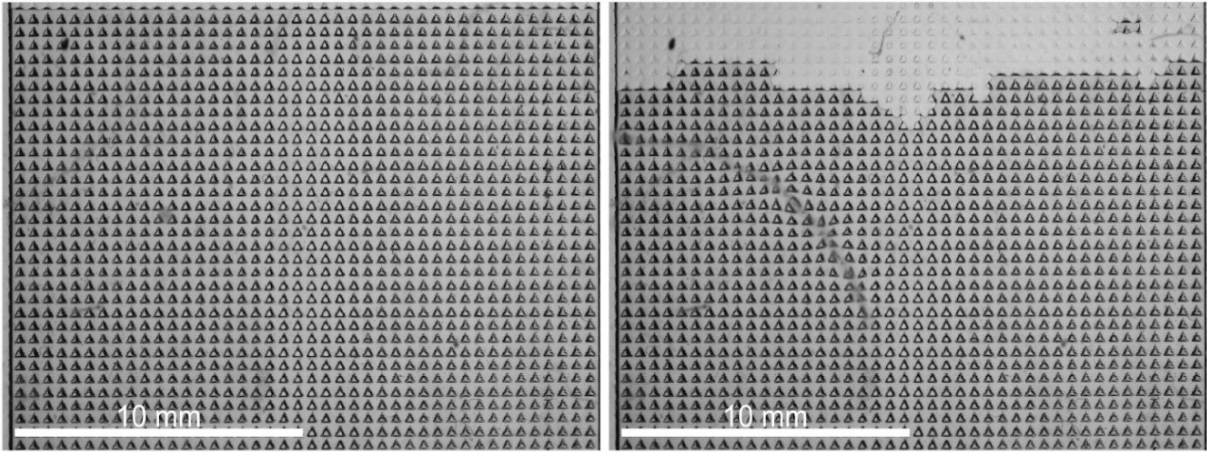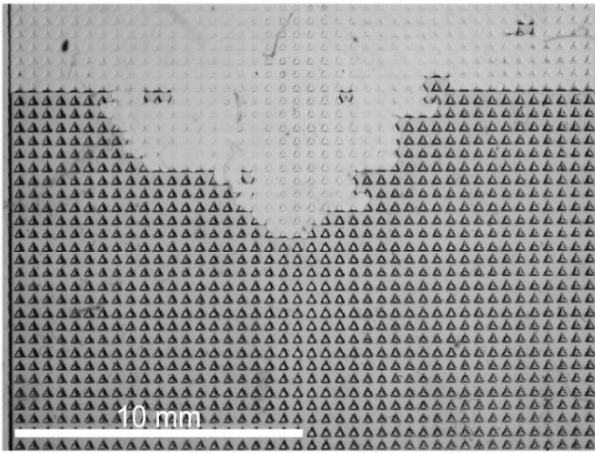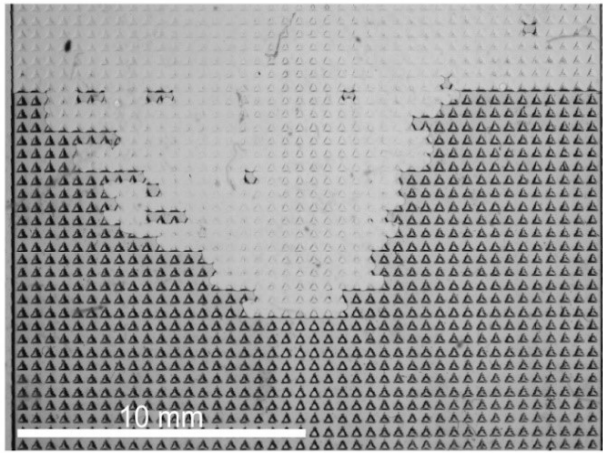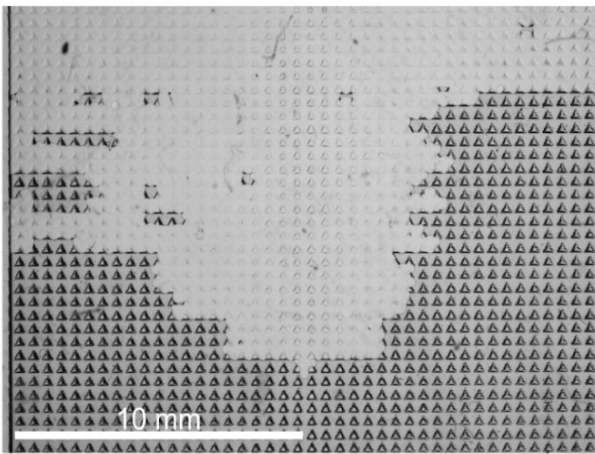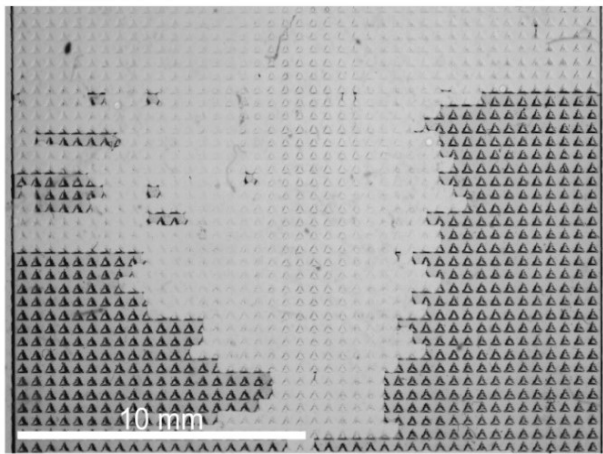
Figure 17 - Example of one of many experiments that is split into intervals for processing. (a) is used as the initial base image and subtracted from (b) through (f); this removes the porous media from the image while keeping the invasion of water into the medium.

| (a) Image Difference | (b) Intensity Filter | (c) Noise Filtered Matrix |
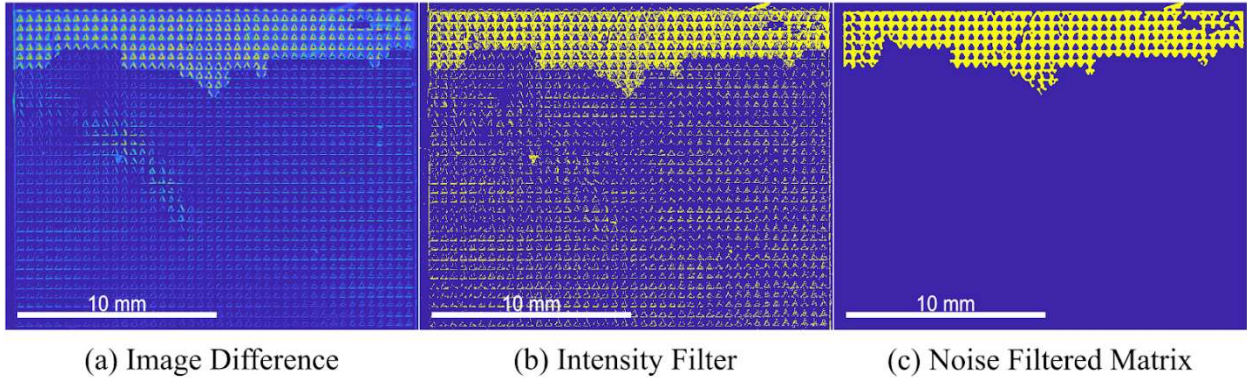
Figure 18 - An example of binary image processing. This process starts with subtracting the initial base image from an interval image, resulting in (a). This yields bright regions of high-intensity values in areas where water has percolated. An intensity filter is applied to distinguish between water and air, resulting in (b). This process turns the image into a binary image. Finally, noise is filtered out in the matrix by removing pixels that don't have many connected components, giving the noise-filtered matrix shown in (c).
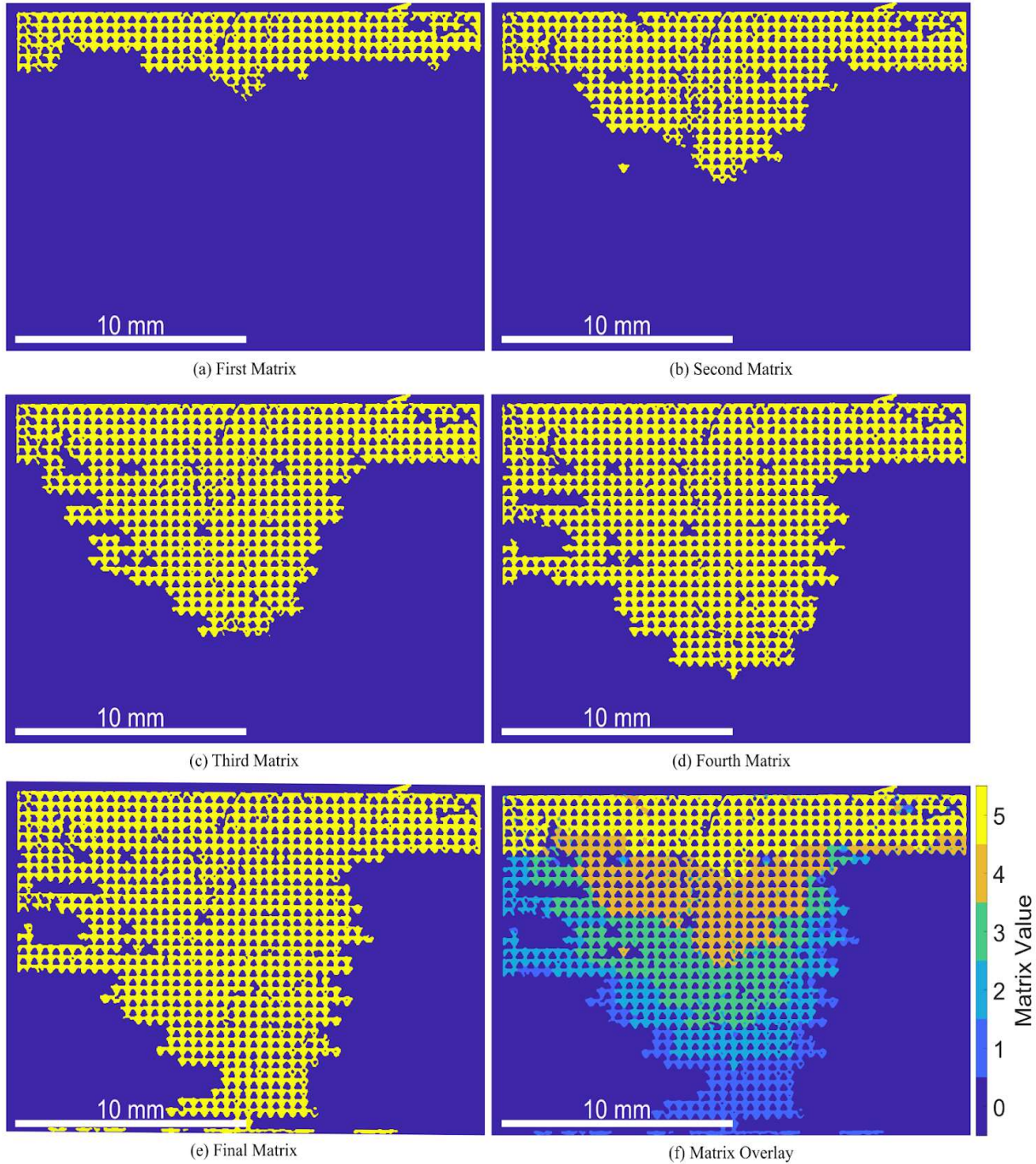
Figure 19 - Example of the final matrix overlay creation process. In this example, we add the five different matrices (a) through (e). Due to the summation, regions within the matrix overlay where water percolated earlier in the experiment have higher values. We use these different values to distinguish between intervals and visualize our experiments over time.
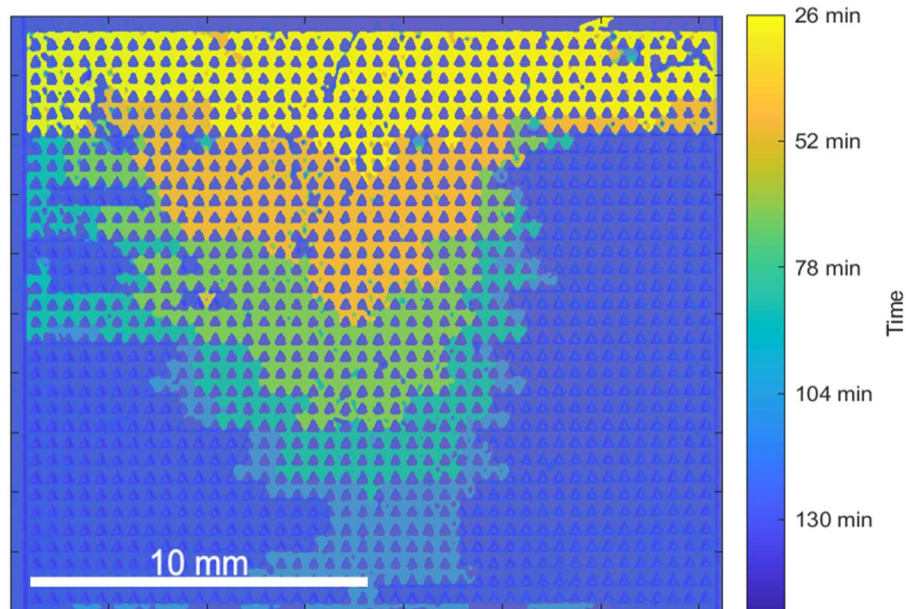
Figure 20 - Overlay of the created matrix onto the original final image. This is done to verify that the filled regions in our final image align appropriately with those in our matrix.

The second set of overlays involves using a set time interval rather than a set number of images. This allows us to retrieve data previously mentioned to use for analysis. The method used to create this overlay is the same as in the visualization case; however, since we analyze data at ten-second intervals and our experiments last upwards of two hours, we don't use it for visualization purposes. The data extracted from the second set of overlays is shown in the following section.

4.4 Quantification of Percolated Water into the Porous Medium

Using the image analysis methods above, 33 of 53 experiments were successfully processed for full data analysis. The rest of the experiments were left out of processing due to extreme amounts of noise even after multiple filtering steps or methodological flaws that may have impacted results (such as not waiting between exposing the device to a vacuum and performing the experiment). Of the 33 processed experiments, 18 were performed in the apex orientation; two were performed at 900 Pa, 11 at 950 Pa, and five at 1000 Pa. For the 15 experiments performed in the base orientation, three were performed at 900 Pa, seven at 950 Pa, and five at 1000 Pa. Table 4 in Appendix A contains all the performed experiments, numbered from 1 to 53, and ordered by increasing pressure. Each external pressure value and orientation shows different percolation effects. We first report results on each pressure and compare them at the end.

The first characteristic of flow we quantify is the pore front of the medium, which refers to the invasion depth (in pores) that the water reaches. There are 33 pore rows inside the medium, but we count the 34th pore row as having exited the medium. Looking at the percolation depth shows whether the media can resist flow at given pressures. This was done with code by finding the largest cluster of pixels in our binary image and identifying the furthest invasion point into the medium. Then, this y-axis coordinate is converted into a pore front value and plotted as a function of time, depending on the interval that correlates to the image studied. It is important to note that, especially at the beginning of the experiment, there can be a lot of noise in the extracted pore front. For this reason, the data is manually parsed through while looking at raw data. If there are significant discrepancies larger than two pores, the pore front values extracted with code are swapped to the pore front shown in the raw data. This is apparent mainly in Figure 21 around the

37

100-minute mark, as these replacements are done using the same value over large instances until the pore front fully invades the next pore.

The following property of the flow we analyze is the saturated volume filled. This is much simpler to extract than the pore front, as we compare the fraction of filled regions to both the filled and unfilled regions and plot as a function of time. With this in mind, if the whole medium is filled, the saturated volume will result in a value of "1". Once these characteristics are studied, we compare them against each other and plot the saturated volume as a function of the pore front. This gives an excellent way to identify whether the flow is uniform, or a fingering effect exists. A more uniform flow will have a higher saturated volume filled with water at lower pore fronts as more of the medium will be filled before percolating; if there is a relatively lower amount of saturated volume filled, it infers the growth of fingers as there will be unfilled regions horizontal to the finger. Lastly, we look at our experiments' flow rate and permeability as a function of time to compare pressure and orientation.

Different experiments are distinguished by color and marker shape in the following sections. Apex orientation experiments are shown in shades of dark blue and light blue, with upwards-pointing triangles. In contrast, base orientation experiments are shown in shades of red and orange with downwards-pointing triangles.

4.4.1 Quantification of Percolated Water at 900 Pa

We observe that in experiments executed at 900 Pa, water cannot percolate through to the other side of the medium in either orientation (base or apex). However, despite little percolation, different trends pertaining to the pore front of the invading fluid between the two orientations still exist, as shown in Figure 21. Percolation in the apex orientation occurs by remaining at one pore front for long periods before flowing forward once more. Conversely, we see that percolation in

the base orientation flows deeper into the medium in a shorter amount of time, and the pore front depth is overall larger than in the apex orientation.
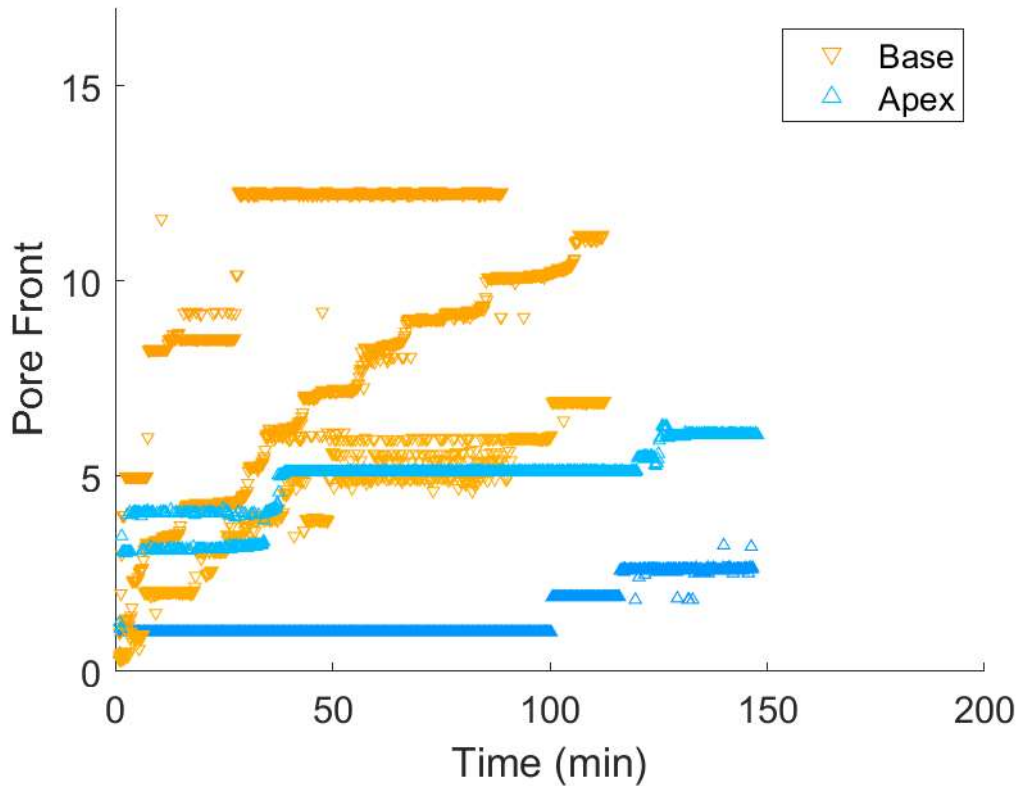
Figure 21 - Pore front depth (in pores) as a function of time for experiments performed at 900 Pa. The pore front depth represents the deepest part of the medium that the invading water was able to percolate into.

Looking at the saturated volume (Figure 22) instead of the pore front reveals that in both orientations, less than one-third of the total volume in the medium is filled by water in our experiments. Interestingly, we see that although the base orientation tends to have a larger pore front depth than the apex orientation, it is not necessarily the same for the saturated volume.
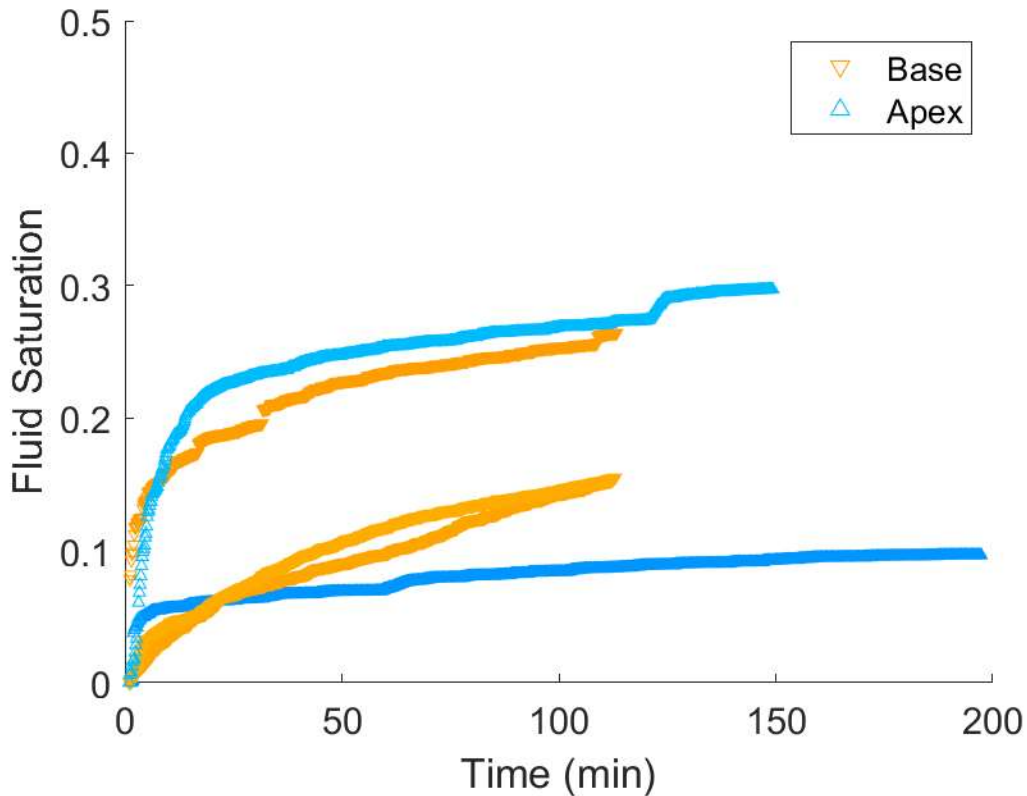
Figure 22 – Normalized Fluid Saturation (with respect to the total volume) as a function of time for experiments performed at 900 Pa.

Finally, looking at the saturated volume as a function of pore depth (Figure 23), we identify a fascinating property of percolation in the two orientations. Although the saturated volume of the medium filled with water is larger in the apex orientation than in the base orientation, the pore front depth is lower. We observe that flow in the apex orientation stops at a pore front and percolates into the medium perpendicular to the flow direction. This means that pores in the same row are likely to be filled as the front advances before the front invades the next row of pores. The opposite happens in the apex orientation; the pore front steadily increases while maintaining a low saturated volume. These results are our first suggestion that fluid fingers' growth depends on the asymmetry of the porous medium. Figure 24 shows an overlay comparison of multiple experiments at 900 Pa.
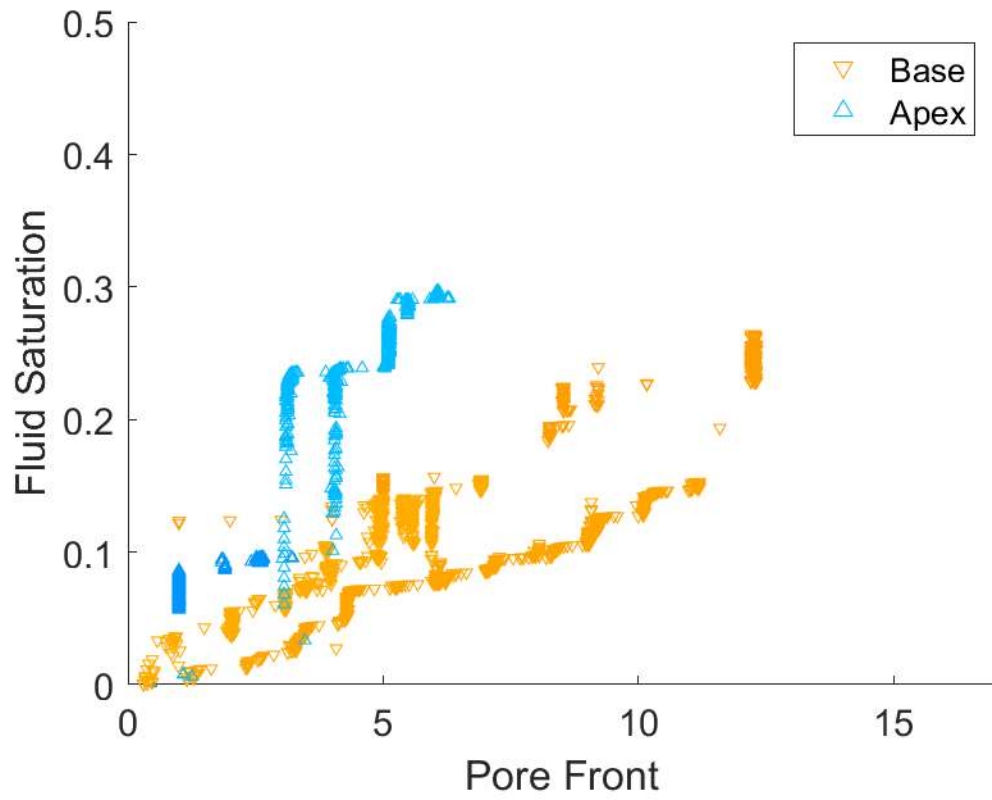
Figure 23 - Normalized Fluid Saturation (with respect to the total volume) as a function of the pore front depth (in pores) for experiments performed at 900 Pa.
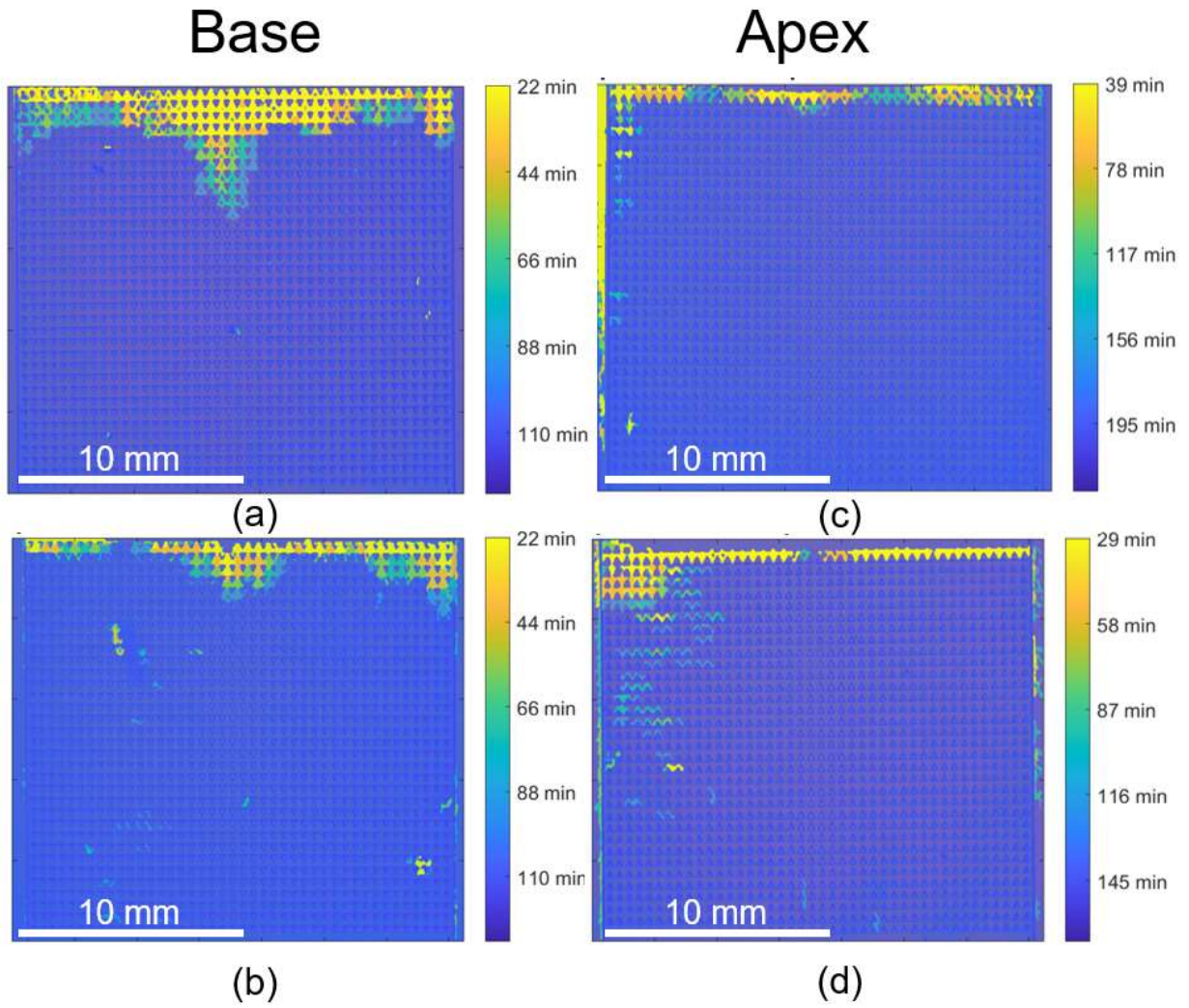
Figure 24 - Comparison of base orientation, (a) and (b), and apex orientation experiments (c) and (d) performed at 900 Pa. Neither orientation allows for much percolation.

4.4.2 Quantification of Percolated Water at 950 Pa

Experiments conducted at 950 Pa have a lot of variability. We observe once again that percolation in the base orientation tends to reach much larger pore front depths in the same amount of time as percolation in the apex orientation (Figure 25). Again, the apex orientation has intermittent flow where the front remains at one pore for long periods before percolating deeper into the medium. Surprisingly, we see similar behavior in the base orientation in one of our experiments. This experiment is highlighted in yellow in Figures 25-27. This observation shows that 950 Pa is very close to a transition pressure where water is more likely to percolate through the medium.
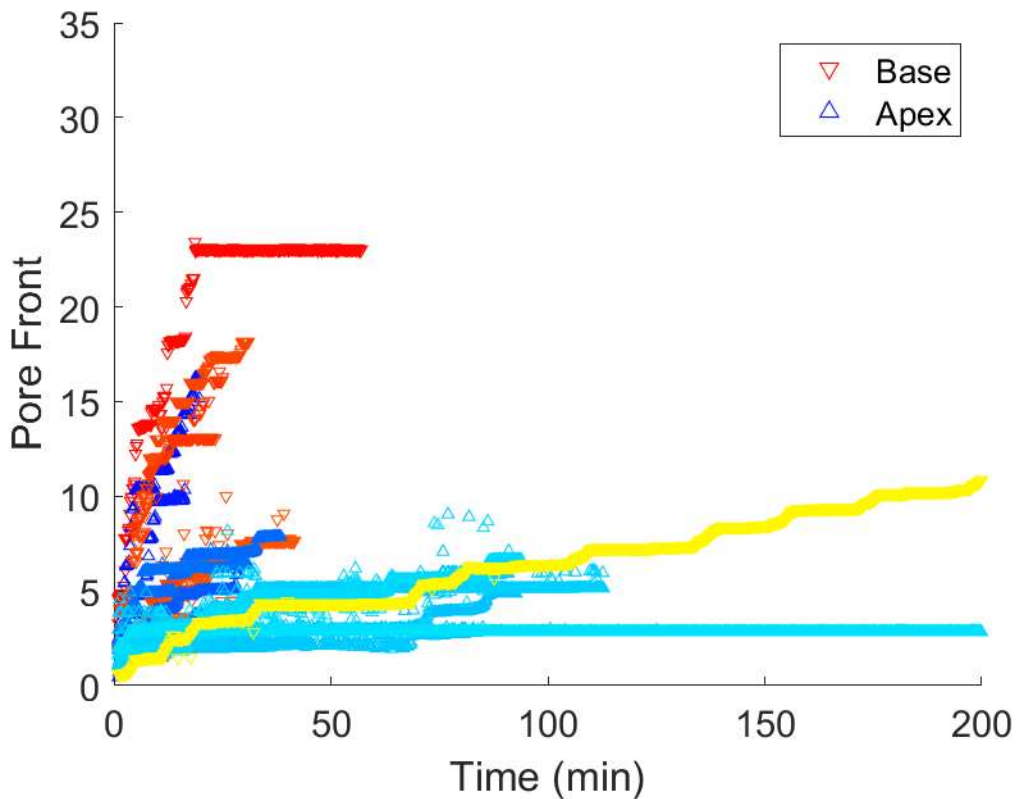
Figure 25 - Pore front depth (in pores) as a function of time for experiments performed at 950 Pa. The data highlighted in yellow represents an experiment in the base orientation that shows apex-like behavior.

When considering the saturated volume in addition to the pore front, it is no surprise that the base orientation tends to reach a higher saturated volume than the apex orientation in the same amount of time (Figure 26). This is due to the base orientation having a larger percolation depth. This additionally supports the idea that 950 Pa is a transition pressure. However, this does not prove that the base orientation is more likely to grow fingers than the apex orientation at this pressure. We must compare the saturated volume at different pore fronts to determine if this is true (Figure 27).
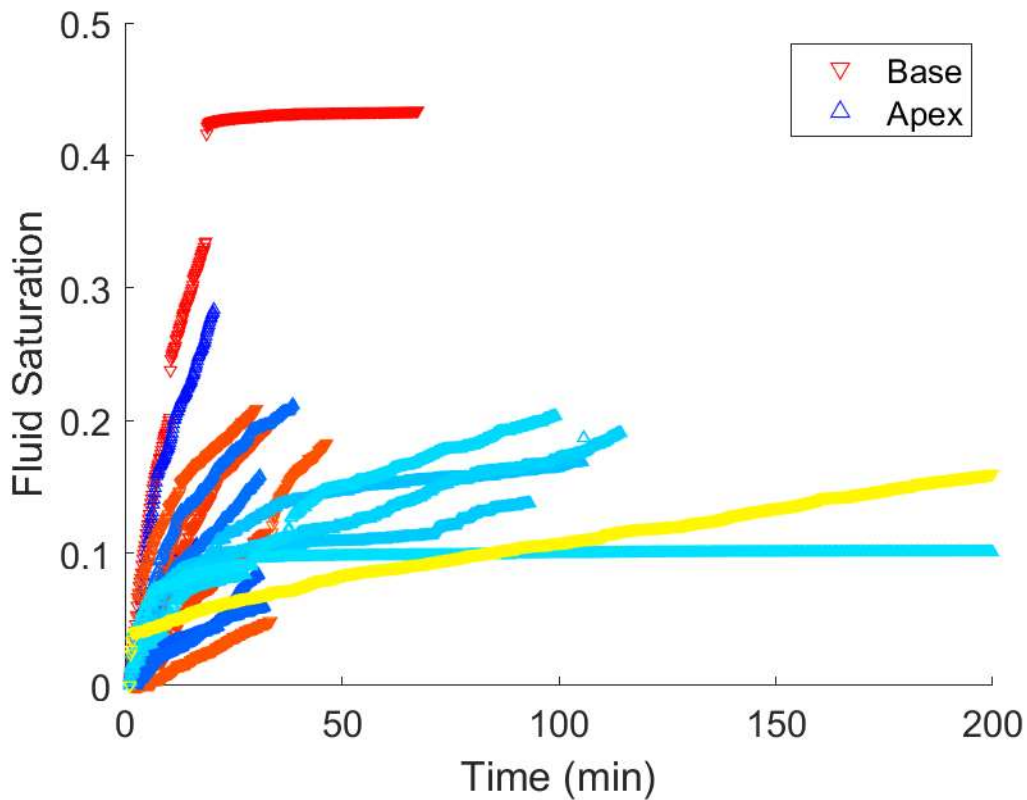
Figure 26 - Normalized Fluid Saturation (with respect to the total volume) as a function of time for experiments performed at 950 Pa.

Even at 950 Pa, with experiments in the base orientation possessing a larger saturated volume than the apex orientation at the same time intervals, we see that the base orientation tends to maintain a lower saturated volume than the apex orientation at the same pore front. This is another factor that reveals that the base orientation is more likely to grow fingers percolate through the medium, while the apex orientation grows a front. Figure 28 shows an overlay comparison of experiments performed in both orientations at 950 Pa showing this exact phenomenon.

Figure 27 - Normalized Fluid Saturation (with respect to the total volume) as a function of the pore front depth (in pores) for experiments performed at 950 Pa. Intriguingly, the data still indicates that the experiment in yellow percolates continuously rather than creating a uniform front due to its linear shape.
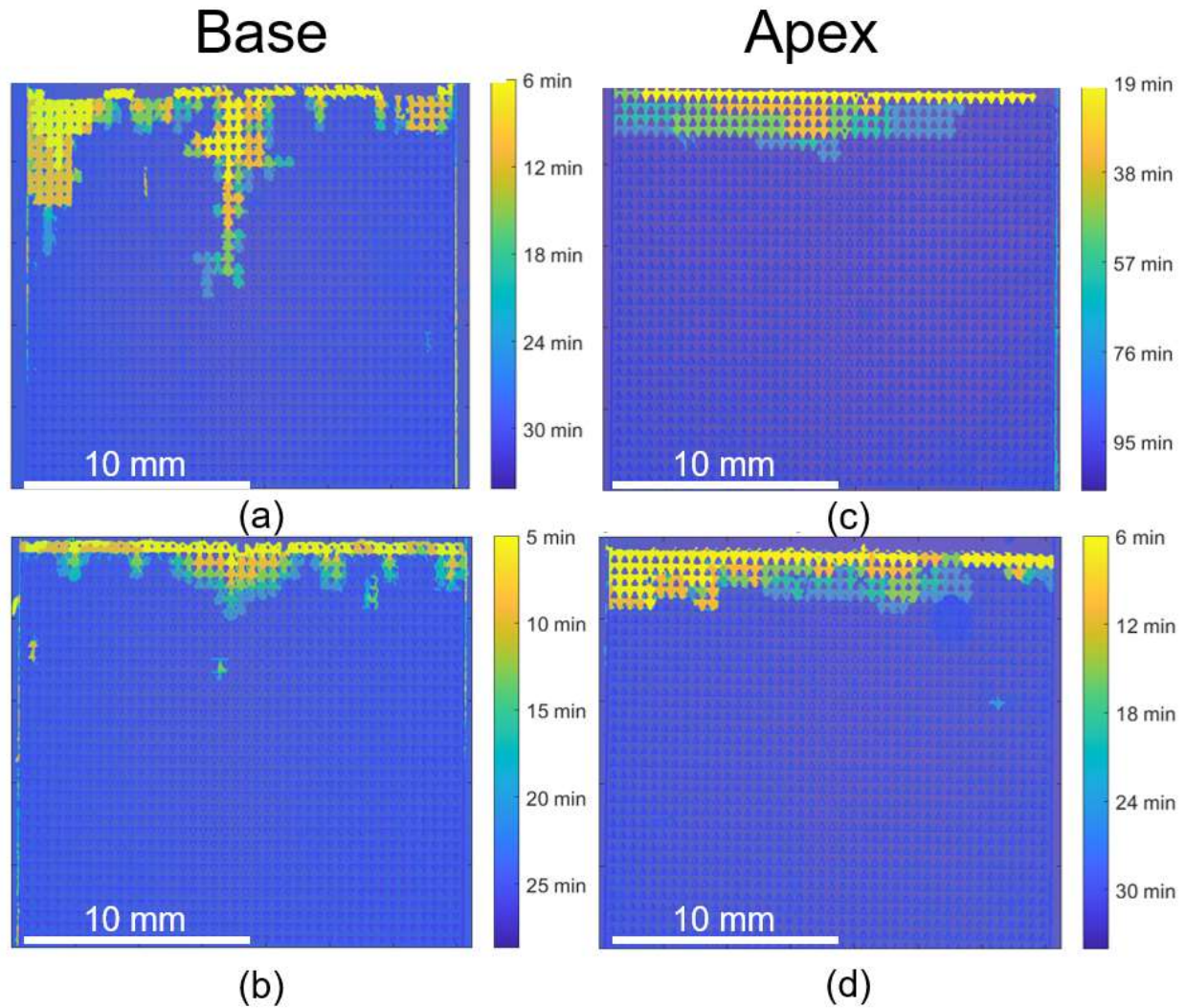
Figure 28 - Comparison of base orientation, (a) and (b), and apex orientation (c) and (d) performed at 950 Pa. Notice the fingering and percolation depth shown in the base orientation. In contrast, the apex orientation shows almost no percolation while maintaining a uniform front.

4.4.3 Quantification of Percolated Water at 1000 Pa

Finally, when studying experiments performed at 1000 Pa, we see that both orientations allow water to percolate entirely through the medium and reach the outlet of our device (Figure 29). Even at this pressure, the apex orientation stays intermittently at one pore front, while the base orientation is much more continuous. The apex orientation takes longer to percolate through the

medium than the base orientation. However, since total percolation is happening in both orientations, we take this as a sign that 1000 Pa is above the transition pressure.
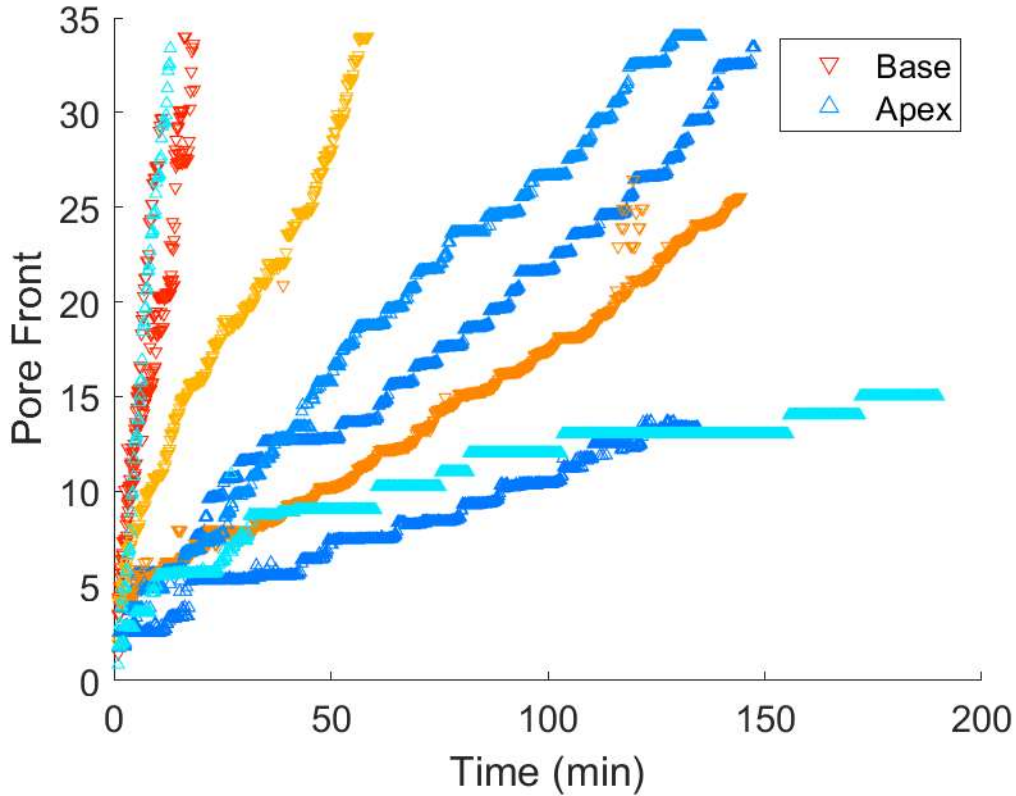
Figure 29 - Pore front depth (in pores) as a function of time for experiments performed at 1000 Pa.

While at 950 Pa, the base orientation has a larger saturated volume since it percolates more than the apex orientation, that argument can no longer be made at 1000 Pa now that both orientations allow percolation. However, as shown in Figure 30, the base orientation tends to have a larger saturated volume earlier in experiments. Once again, we must look at the saturated volume as a function of the pore front to further interpret our observations.
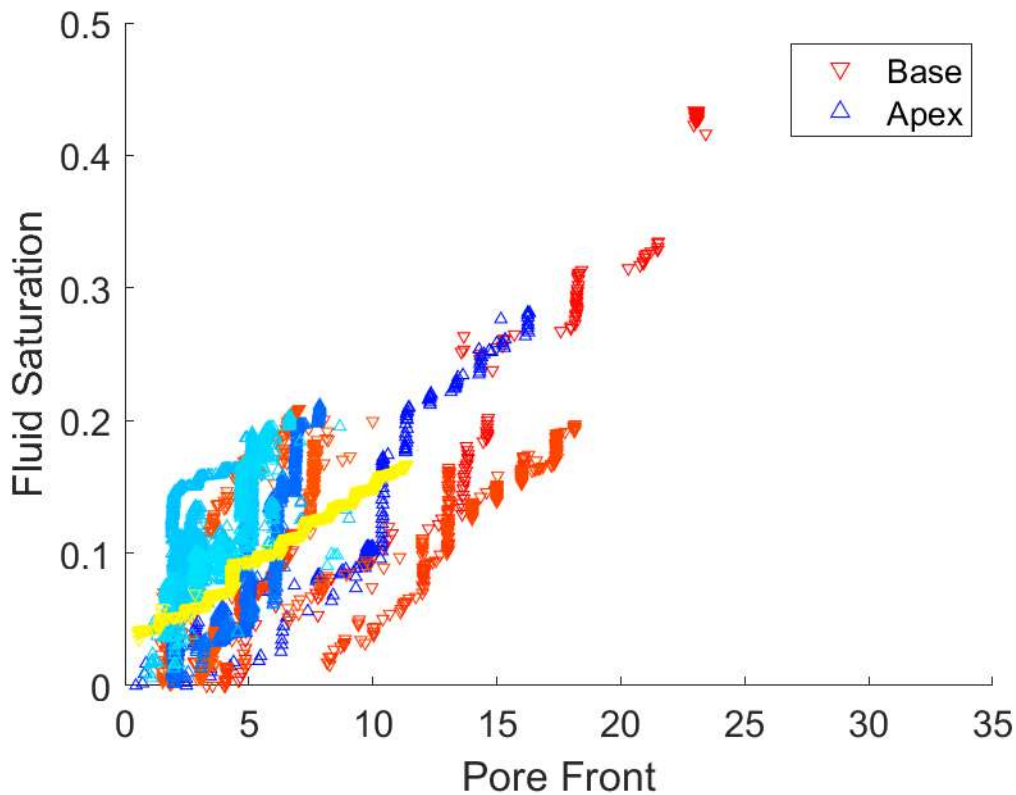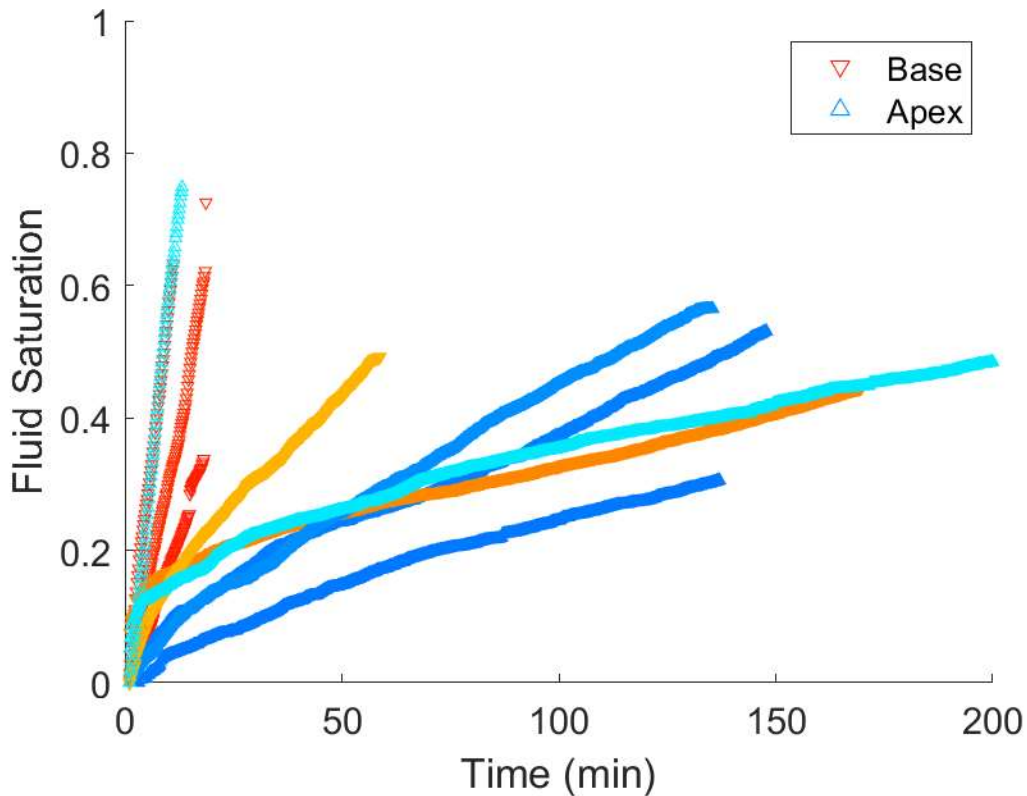
Figure 30 - Normalized Fluid Saturation (with respect to the total volume) as a function of time for experiments performed at 1000 Pa.

Studying the difference in saturated volume between the two orientations in Figure 31 reveals that when both orientations reach the same depth, the apex orientation is more likely to have a larger front spread across the whole medium. When fully invaded, the apex orientation fills more than half of the saturated volume, while the base orientation is scattered. This is likely due to the asymmetry imposing a fingering effect in the base orientation as opposed to a uniform front in the apex orientation. Figure 32 shows an overlay comparison of experiments performed in both orientations at 1000 Pa.
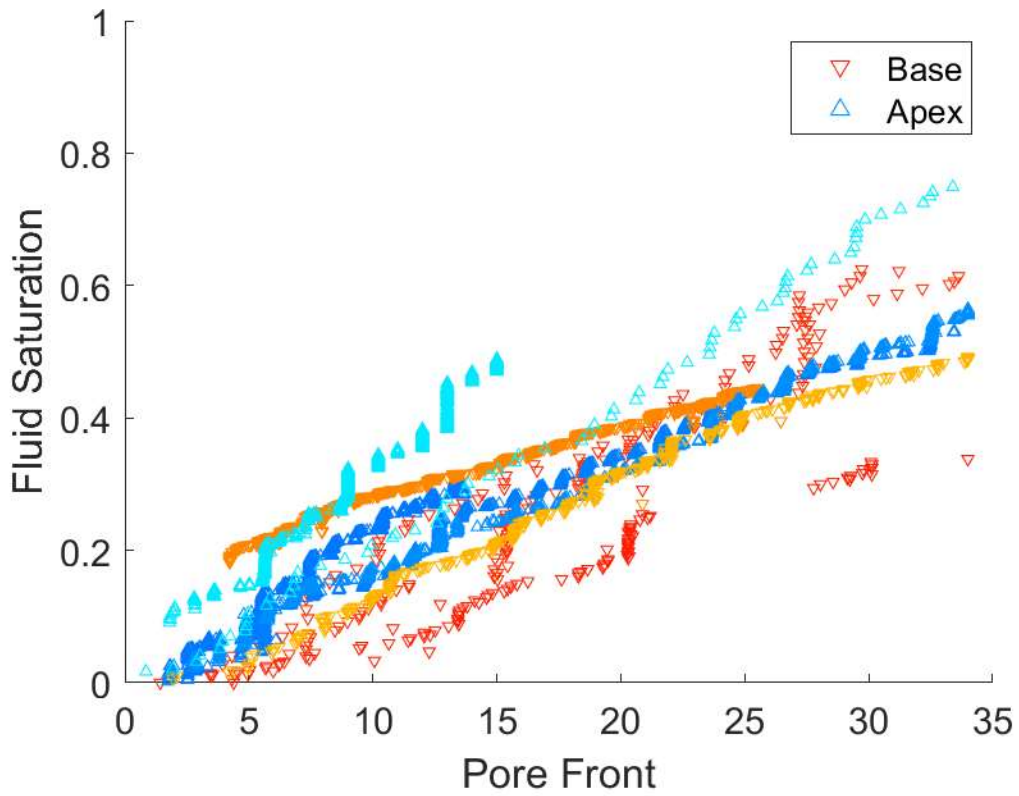
Figure 31 - Normalized Fluid Saturation (with respect to the total volume) as a function of the pore front depth (in pores) for experiments performed at 1000 Pa.
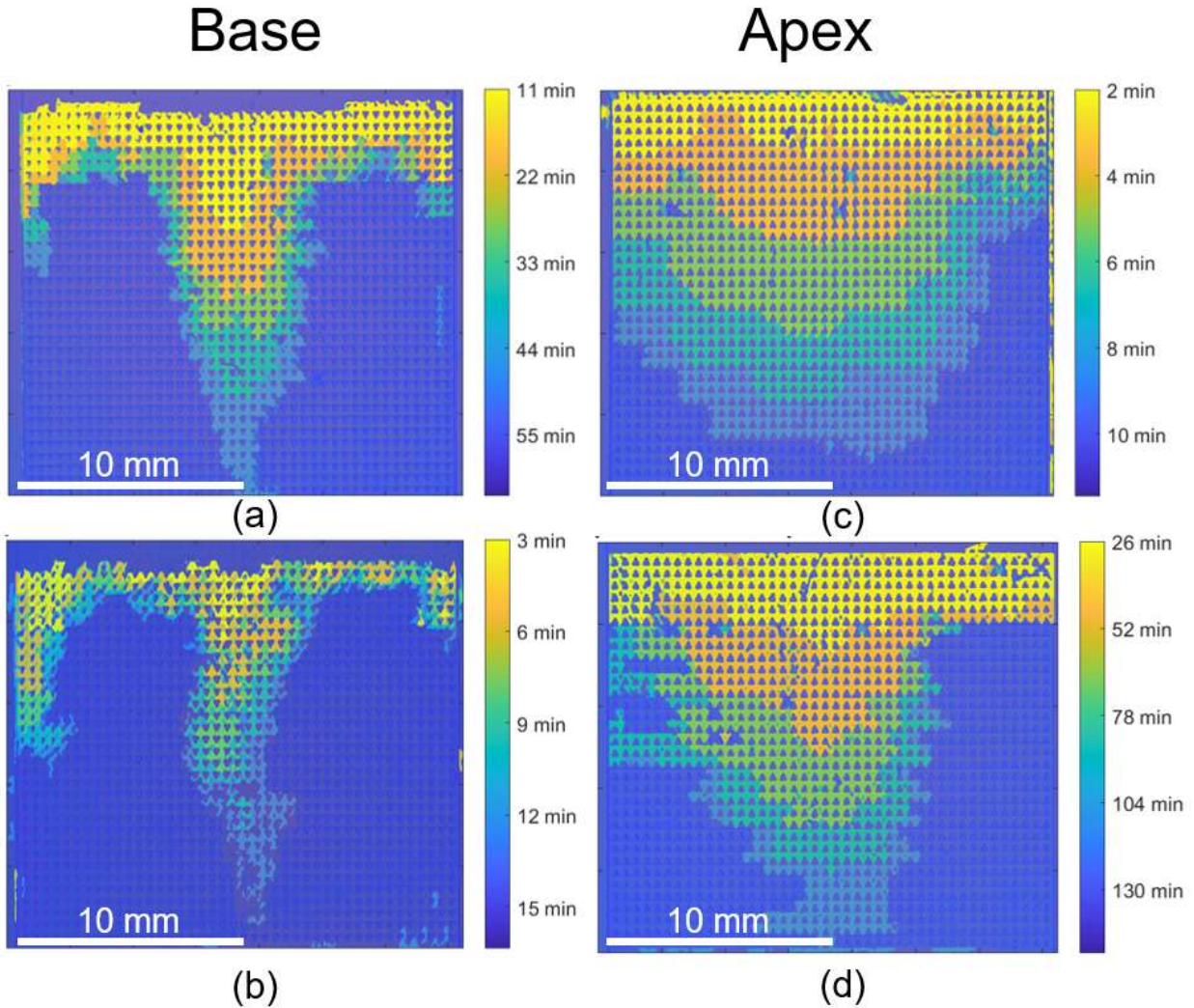
Figure 32 - Comparison of base orientation experiments (a) and (b), and apex orientation experiments (c) and (d) performed at 1000 Pa. Notice the difference between the finger growth in the base orientation and the front growth in the apex orientation.

4.4.4 Quantification Comparison between 900 Pa, 950 Pa, and 1000 Pa

Overall, we observe that the invading fluid percolates deeper into the medium when the triangular pillars are in the base orientation than in the apex orientation. However, there also exists a difference in invasion dynamics. As seen in Figure 33 (a), while it is true that at the same pressures, the base orientation has an overall higher average pore front depth than the apex

orientation, it does not necessarily mean that it has a higher saturated volume, as seen in Figure 33 (b).
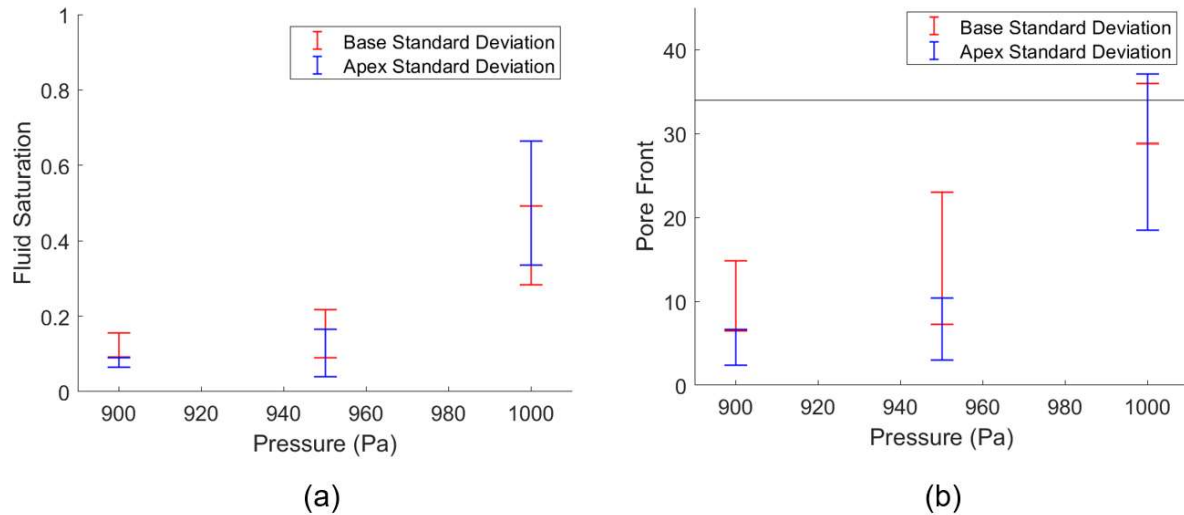
Figure 33 - Comparison of expected values at the end of experiments regarding fluid saturation (a) and pore front (b) for the two different orientations as functions of pressure. Notice that the apex orientation has a tight distribution and low value at 900 Pa. At the same time, it drastically increases at 1000 Pa with a much wider spread, surpassing the average saturated volume occupied in the base orientation.

The base orientation experiments show that water fills a very low saturated volume, with most experiments below 1000 Pa not filling one-third of the medium. Most of our experiments at 1000 Pa also show less than half of the medium being filled. This is interesting because, as we've seen previously, most of our experiments at 1000 Pa have percolated through the whole medium. Additionally, there is a significant scattering of percolation depth at 950 Pa, yet here we see a tight spread.

We again see a tight spread for 900 Pa and 950 Pa when cataloging the experiments performed in the apex orientation. Experiments below 1000 Pa don't fill more than one-third of the

medium. However, there is a large spread at 1000 Pa, with experiments filling between 24% and 75% of the medium.

Comparing data from the two orientations, we see that flow in the base orientation is more likely to fill less saturated volume than the apex when, in both cases, water has reached the other side of the medium during the experiment. As pressure increases, the base orientation allows for invasion first with fingers, and the apex orientation allows for invasion with a front. Table 3 summarizes the findings at the end of our experiments for both orientations at each pressure value.

Table 3 - Average Values and Standard Deviations for each Orientation's Invasions

Pressure	Base Orientation Pore Front Depth	Base Orientation Fluid Saturation	Apex Orientation Pore Front Depth	Apex Orientation Fluid Saturation
900 Pa	10.7 ± 4.2 pores	12.4 ± 3.1 %	4.5 ± 2.1 pores	7.8 ± 1.2
950 Pa	15.1 ± 7.9 pores	15.4 ± 6.4 %	6.7 ± 3.7 pores	10.3 ± 6.2
1000 Pa	32.4 ± 3.6 pores	38.8 ± 10.4 %	27.8 ± 9.3 pores	50 ± 16.4 %

We can quantify the volumetric flow rate over time by converting the fluid saturation over time data we extracted for all pressures shown in the above section (Figures 34 – 36). This is done by calculating the difference in fluid saturation between one time interval and the next, multiplying the fluid saturation by the volume of space in the device, and dividing it by the ten-second time

interval. Once calculated, we plot the average volumetric flow rate over intervals of ten minutes over time.
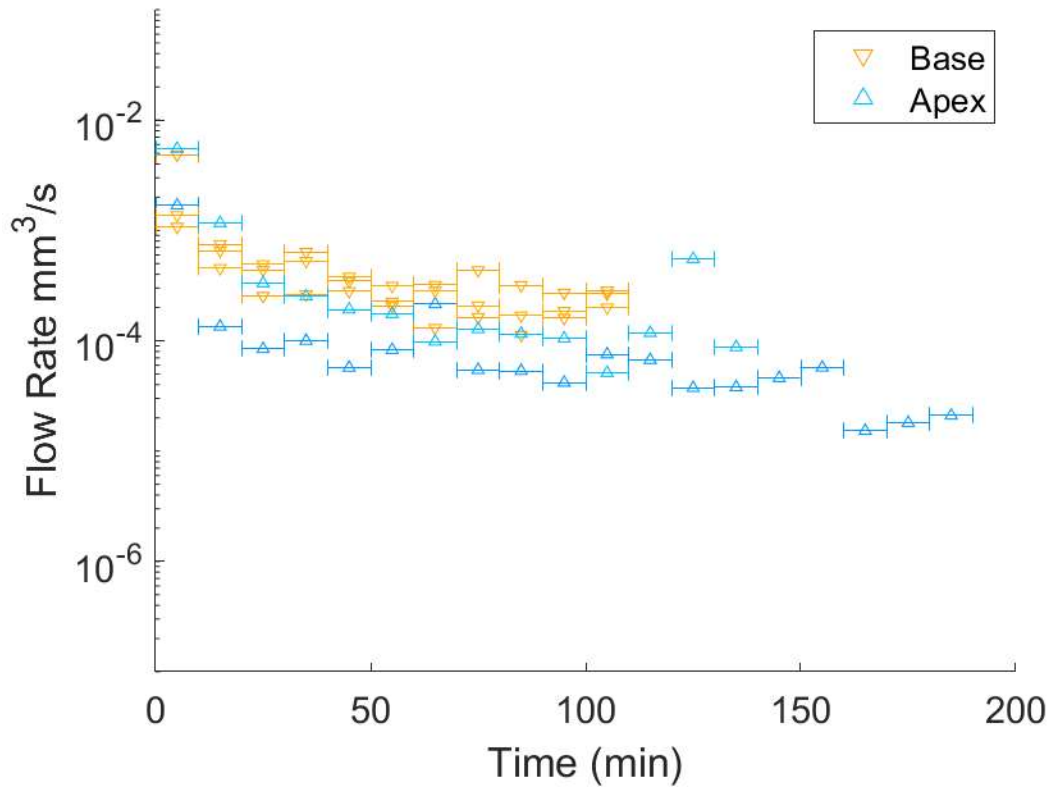
Figure 34 - Average flow rate over ten-minute intervals as a function of time for experiments performed at 900 Pa. The horizontal bars represent the ten minute intervals used to average the data.
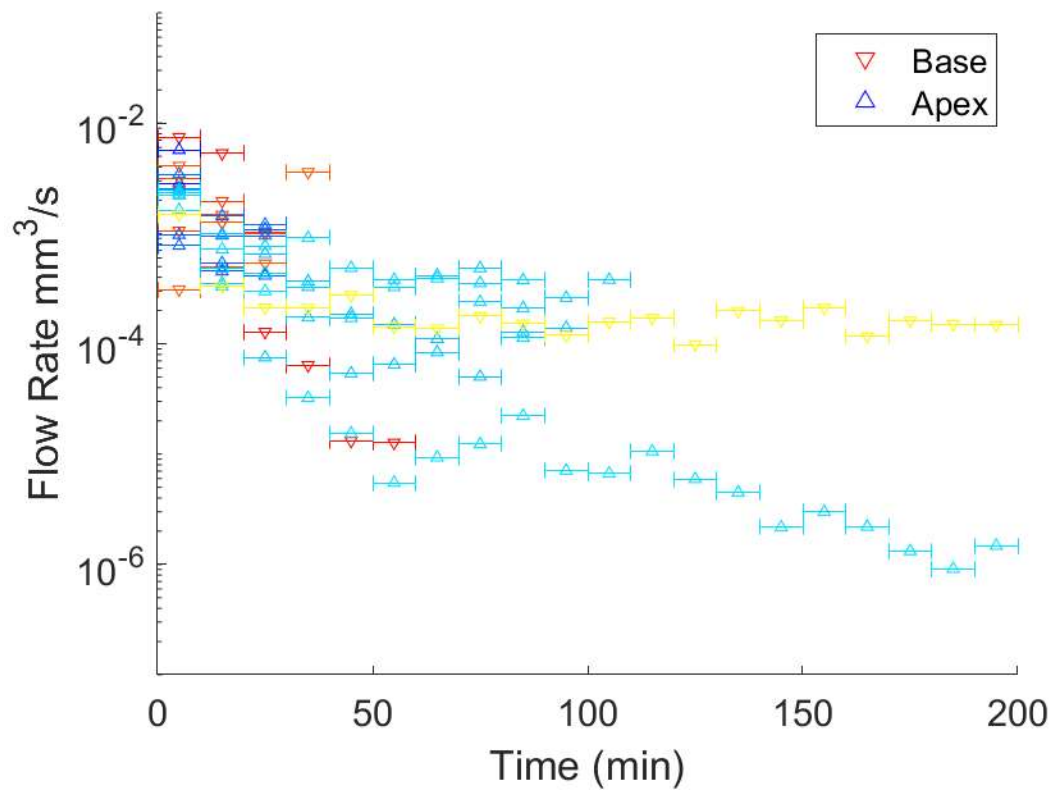
Figure 35 - Average flow rate (a) and permeability (b) over ten-minute intervals as a function of time for experiments performed at 950 Pa.
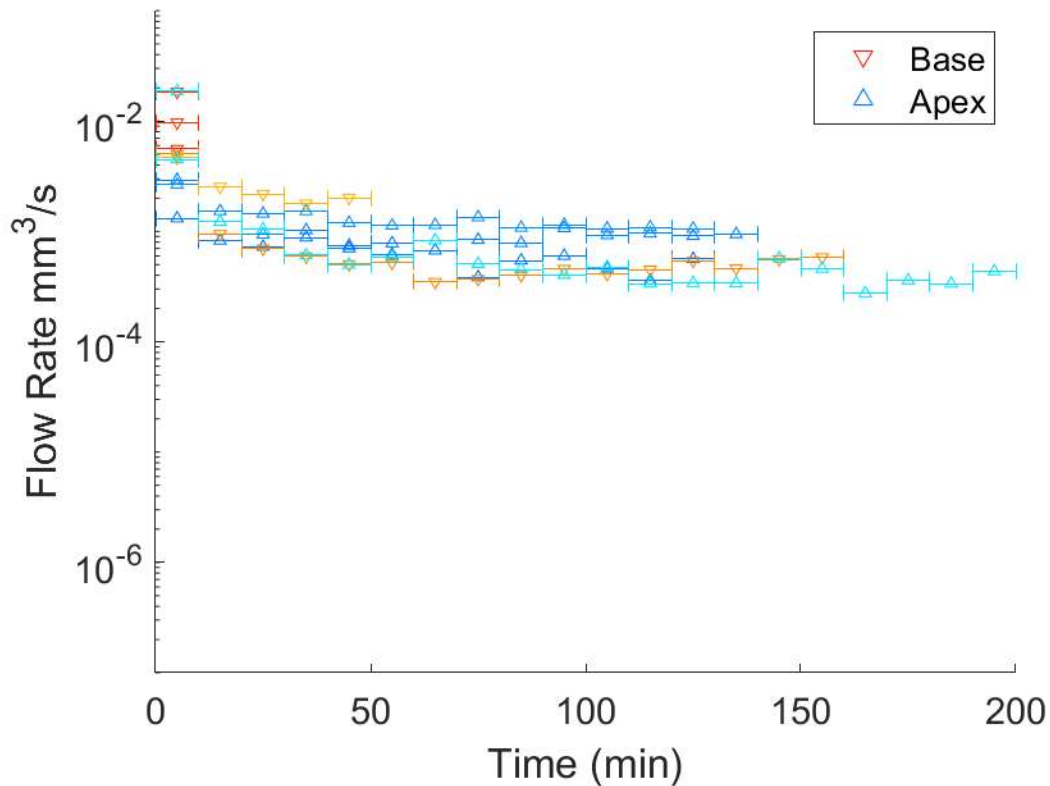
Figure 36 - Average flow rate (a) and permeability to water (b) over ten-minute intervals as a function of time for experiments performed at 1000 Pa.

Notice that the flow rate and water permeability share a striking pattern resemblance at all pressures; water invades the medium at flow rates around 10^{-2} mm^3/s in either direction of invasion with respect to triangle orientation. Interestingly, the flow rate decreases with the largest reduction at the lowest pressure (900 Pa). Out of these experiments, the ones in the base orientation tend to have a higher flow rate at experiment conclusion than those in the apex orientation. Additionally, the base orientation experiment highlighted in yellow maintains a constant flow rate throughout the experiment, supporting this idea. At these two pressures, since the flow rate decreases, the medium's permeability to water (a relative permeability to water and air) has decreased. Finally, experiments at 1000 Pa maintain their flow rate throughout the allotted time much more than those performed at 900 Pa and 950 Pa.

Appendix A has a table highlighting all experiments executed during the research period. Note that the ones not used in the analysis were discarded due to excessive noise or methodological flaws. The experiments used in the study were all performed with devices exposed to the same vacuuming time and rest time pre-submersion in water and experiment execution. Additionally, the table contains the device number that was used. However, this was only kept track of after the 20th experiment. Since we reuse the devices, we record which device was used for which experiment to prevent any complications concerning device reliability. As it stands, device #1 was tossed due to channel leakage. This can happen for several reasons, but most likely occurs when the two pieces in a device fail to completely bond to each other.

4.5 Additional Comments and Observations

We briefly looked at other geometries during this study. One of these consisted of doubling the height of the triangular pillars (Figure 37). This yielded very different invasion dynamics than the original orientation shown in the previous analysis. Interestingly, while we only ran two experiments in the base orientation and one in the apex orientation, both orientations were more likely to fill pores perpendicular to the flow direction before traveling deeper into the medium. There was no finger growth in the base orientation. However, it seemed to grow much faster.
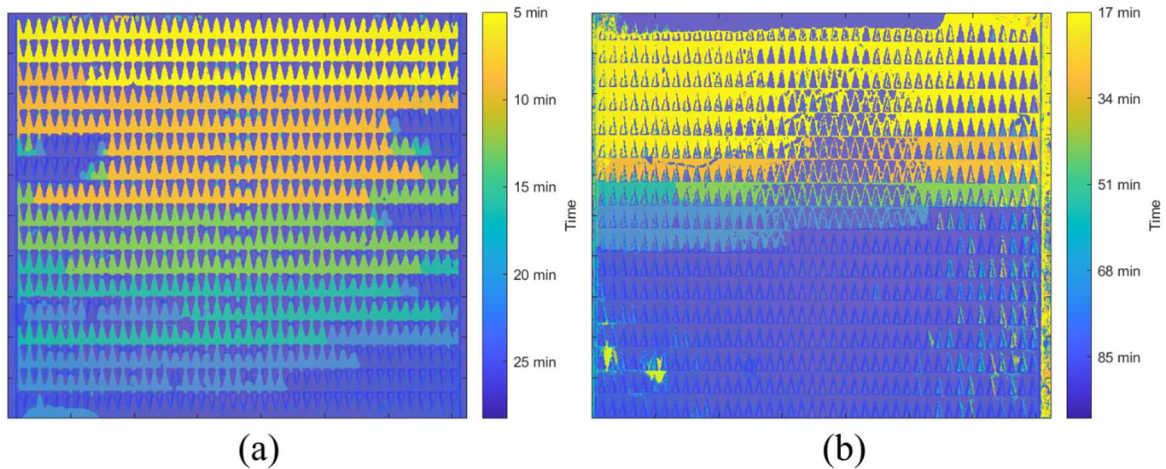
Figure 37 - Comparison of experiments performed in each orientation with the elongated triangular pillars. Notice that percolation in the base orientation (b) fills most of the medium, as opposed to experiments with the original geometry. The percolation in the apex orientation fills every pore as the fluid flows deeper into the medium.

Earlier experiments were performed at a smaller pillar size with a different, smaller medium (Figure 38). The triangular pillars in this design had a 210 μm side length instead of 390 μm, and the medium was only 24 rows deep instead of 34. With these dimensions, we noticed that the triangular properties of the pillars were being overwhelmed by the meniscus size and being treated as a point. This is also partly due to the pixelation effect caused by the 3D printer. Notably, we also observed that the fluid started invading the medium before coming into contact with the whole porous boundary.
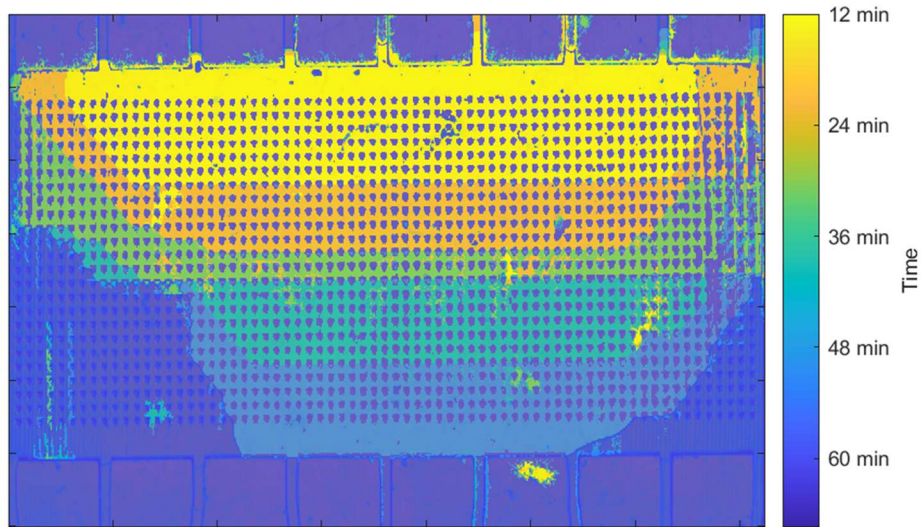
Figure 38 - Overlay of the experiment conducted in the base orientation with smaller dimensions (a 210 μm triangle side length). This geometry was used in early testing and quickly modified to improve experiments.

We adjusted the size of the triangles to a side length of 390 μm and developed a new design consisting of 12 rows and 42 columns. This design seemed to work initially, showing results that now contradict our final findings. Flow in the apex orientation (Figure 39) was likelier than in the base orientation (Figure 40). These previous experiments were found at 1000 Pa - 1200 Pa rather than 800 Pa - 1000 Pa. However, we still see growth of fingers in the base orientation and a front in the apex orientation. After reviewing the design, we realized that the branch width might have been the limiting factor affecting flow into the medium. The width of these branches was less than the width between pores. In addition, they were not made according to the 30 μm printer resolution. The branches were widened to the most recent design, and the porous media was placed deeper into the device while increasing the rows to 34. After this change, we found that experiments were more consistent with each other, and water was able to flow through the medium at lower pressures. We believe that increasing the number of rows and the branch width has led to this reversal in results.
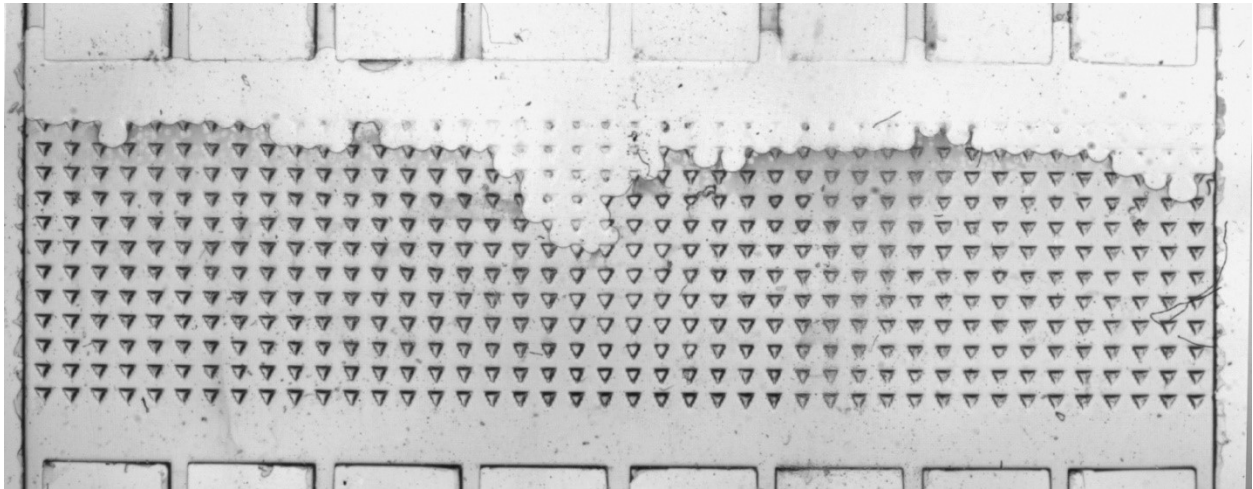
Figure 39 - Final state of a 60-minute experiment in the base orientation at 1200 Pa. This design's branch width (270 μm) is much less than the branch width in newer experiments (450 μm). This orientation prevents flow under these conditions with these dimensions.

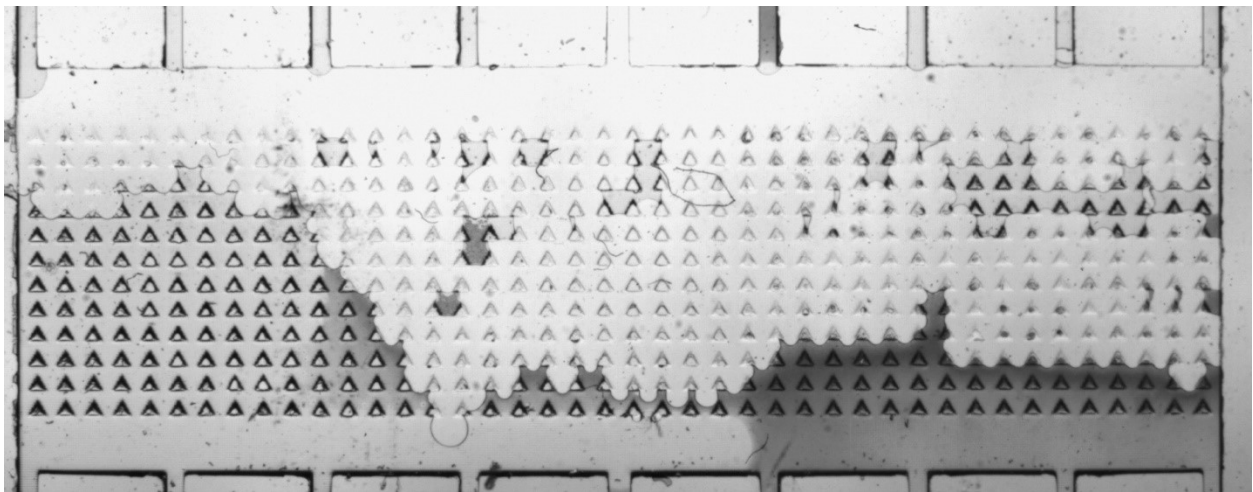Figure 40 - Final state of a 60-minute experiment in the apex orientation at 1200 Pa. This orientation allows flow under these conditions with these dimensions.

5.0 Conclusions

We experimentally investigate the impact of asymmetry of the porous medium's structure on fluid-fluid displacement. The porous medium consists of a matrix of triangular pillars (with a 390 μm side length) between two plates separated by a 90 μm gap. We use standard soft-lithography and microfluidic techniques to fabricate the porous medium. The medium is initially filled with air, which will be displaced by water at a constant pressure provided by a hydrostatic pressure head. Using a wide-field optical microscope, we observe the fluid's displacement and track the medium's invasion over time.

Immiscible displacement can only occur if the viscous pressure of the invading fluid (water) is greater than the capillary pressure of the resident fluid (air). We find that the threshold for invasion of the medium with water is approximately 950 Pa. Our experimental investigation shows a fluid front can develop between air and water in the porous medium. Depending on the direction of injection of water with respect to the orientation (apex versus base) of the triangles in the medium, the width of this fluid front varies. The width of the fluid front during apex invasion is wider than the fluid front during base invasion, above the threshold pressure for invasion. Interestingly, the fluid front during base invasion resembles a viscous finger, as seen in the displacement of a low-viscosity fluid. The invaded volume in the apex orientation is larger than that in the base orientation at the same pore front for all applied pressures: I. 900 Pa (below invasion), II. 950 Pa (near the invasion threshold), and III. 1000 Pa (above the invasion threshold). These three pressure regimes are proven through our experimental measurements. Additionally, due to the development of fingers, the base orientation allows for deeper percolation in a shorter amount of time than the apex orientation. At pressures above the invasion threshold, the base orientation fills up less of the medium than the apex orientation.

We measure the flow rate by calculating the changes in the volume of the fluid (water) in the medium over time from our microscope images. At all pressures, water invades the medium at flow rates around 10^{-2} mm^3/s in either direction of invasion with respect to triangle orientation. Interestingly, the flow rate decreases with the largest reduction at the lowest pressure (900 Pa). The flow rate for water approaches 10^{-3} mm^3/s when the external pressure is 1000 Pa; a constant flow rate during invasion is expected above the invasion threshold. By contrast, the flow rate of the invading fluid at a constant pressure of 950 Pa (close to the invasion threshold) decreases at a faster rate, and after 40 minutes, the flow rate drops below 10^{-4} mm^3/s (which is smaller than the constant flow rate for a full invasion). In the time scale of these experiments, the flow is impeded by the medium. We further verify this observation by plotting the flow rate versus the percolation depth.

Future work regarding this research is very flexible. Many changes can be made to the dimensions and size of the porous medium. These changes may even include varying the size of the pillars, inserting faults, or changing the 2D structure into a 3D one. Another part that requires study is extending the duration of experiments to upwards of 24 hours to identify whether the flow is genuinely impeded below the threshold pressure or is just dramatically slowed down.

Appendix A

Table 4 - All Experiments Arranged by Increasing Pressure

Exp. #	Device #	Orientation	Pressure (Pa)	Time (min)	Used in Analysis
21	1	Base	800	6	No
22	2	Base	800	11	No
`23	3	Base	800	48	No
24	4	Base	800	18	No
9	Unknown	Apex	850	15	No
40	2	Apex	900	190	Yes
41	3	Base	900	110	Yes
42	4	Base	900	110	Yes
43	2	Base	900	110	Yes
45	3	Apex	900	150	Yes
3	Unknown	Base	950	9	No
4	Unknown	Base	950	11	No
5	Unknown	Base	950	23	No

6	Unknown	Base	950	68	Yes
7	Unknown	Apex	950	20	Yes
8	Unknown	Apex	950	15	Yes
10	Unknown	Apex	950	11	No
26	1	Base	950	22	No
27	3	Base	950	25	Yes
28	5	Base	950	30	Yes
29	3	Base	950	30	Yes
30	5	Base	950	29	Yes
31	2	Base	950	45	Yes
32	5	Apex	950	30	Yes
33	2	Apex	950	30	Yes
34	6	Apex	950	30	Yes
35	4	Apex	950	30	Yes
46	2	Apex	950	105	Yes
47	4	Apex	950	90	Yes

48	3	Apex	950	110	Yes
49	5	Apex	950	100	Yes
50	6	Apex	950	200	Yes
53	2	Base	950	450	Yes
2	Unknown	Base	1000	10	No
11	Unknown	Base	1000	3	No
12	Unknown	Base	1000	3	No
13	Unknown	Base	1000	5	No
14	Unknown	Base	1000	18	Yes
15	Unknown	Base	1000	3	No
16	Unknown	Base	1000	20	No
17	Unknown	Base	1000	10	Yes
18	Unknown	Base	1000	8	No
19	Unknown	Base	1000	19	Yes
36	2	Apex	1000	140	Yes
37	4	Apex	1000	150	Yes

38	2	Base	1000	170	Yes
39	4	Apex	1000	140	Yes
44	4	Base	1000	60	Yes
51	4	Apex	1000	560	Yes
52	4	Apex	1000	12	Yes

References

[1] Primkulov, B., Pahlavan, A., Fu, X., Zhao, B., MacMinn, C., & Juanes, R. (2021). "Wettability and Lenormand's diagram". Journal of Fluid Mechanics, 923, A34. doi:10.1017/jfm.2021.579

[2] White, Frank M. (2011). Fluid Mechanics (7th ed.). McGraw-Hill. ISBN 978-0-07-352934-9.

[3] Schroeder, Daniel V., An Introduction to Thermal Physics (Oxford, 2021; online edn, Oxford Academic, 18 Mar. 2021), https://doi.org/10.1093/oso/9780192895547.001.0001, accessed 1 Feb. 2024.

[4] Squires TM, Quake SR (2005). "Microfluidics: Fluid physics at the nanoliter scale" (PDF). Reviews of Modern Physics. 77 (3): 977–1026. Bibcode:2005RvMP...77..977S. doi:10.1103/RevModPhys.77.977.

[5] Niculescu AG, Chircov C, Bîrcă AC, Grumezescu AM. Fabrication and Applications of Microfluidic Devices: A Review. Int J Mol Sci. 2021 Feb 18;22(4):2011. doi: 10.3390/ijms22042011. PMID: 33670545; PMCID: PMC7921936.

[6] Pawell Ryan S (2013). "Manufacturing and wetting low-cost microfluidic cell separation devices". Biomicrofluidics. 7 (5): 056501.

[7] Mingchao Liu, Si Suo, Jian Wu, Yixiang Gan, Dorian A. H. Hanaor, et al.. Tailoring porous media for controllable capillary flow. Journal of Colloid and Interface Science, 2019, 539, pp.379-387. ff10.1016/j.jcis.2018.12.068ff. Ffhal-02310722f

[8] Saurabh, Suman (2022-02-15). "Flow regime evolution and stress-dependent permeability in nanoporous rocks". Fuel. Elsevier. 310: 122413. doi:10.1016/j.fuel.2021.122413. S2CID 243474407.

[9] Bear, Jacob (2013-02-26). Dynamics of fluids in Porous Media. ISBN 9780486131801.

[10] Venzac, B., Liu, Y., Ferrante, I. et al. Sliding walls: a new paradigm for fluidic actuation and protocol implementation in microfluidics. Microsyst Nanoeng 6, 18 (2020). https://doi.org/10.1038/s41378-019-0125-7

[11] Weibel DB, Kruithof M, Potenta S, Sia SK, Lee A, Whitesides GM. Torque-actuated valves for microfluidics. Anal Chem. 2005 Aug 1;77(15):4726-33. doi: 10.1021/ac048303p. PMID: 16053282.

[12] Local Pore Size Correlations Determine Flow Distributions in Porous Media

Karen Alim, Shima Parsa, David A. Weitz, and Michael P. Brenner

Phys. Rev. Lett. 119, 144501 – Published 3 October 2017

[13] Trojer, Mathias & Szulczewski, Michael & Juanes, Ruben. (2015). Stabilizing Fluid-Fluid Displacements in Porous Media Through Wettability Alteration. Physical Review Applied. 3. 10.1103/PhysRevApplied.3.054008.

[14] Yanying Feng, Zhaoying Zhou, Xiongying Ye, Jijun Xiong, Passive valves based on hydrophobic microfluidics, Sensors and Actuators A: Physical, Volume 108, Issues 1–3, 2003, Pages 138-143, ISSN 0924-4247

[15] Asymmetric invasion in anisotropic porous media Dario Maggiolo, Francesco Picano, and Federico Toschi Phys. Rev. E 104, 045103 – Published 14 October 2021

[16] Feldman, D. Polymer History. Des. Monomers Polym. 2008, 11, 1–15, doi:10.1163/156855508x292383.

[17] Rodrigues, R.O.; Lima, R.; Gomes, H.T.; Silva, A.M.T. Polymer microfluidic devices: an overview of fabrication methods. U. Porto J. Eng. 2015, 1, 67–79, doi:10.24840/2183-6493_001.001_0007.

[18] Wolf, M.P.; Salieb-Beugelaar, G.B.; Hunziker, P. PDMS with designer functionalities—Properties, modifications strategies, and applications. Prog. Polym. Sci. 2018, 83, 97–134, doi:10.1016/j.progpolymsci.2018.06.001.

[19] Sun, J.; Li, Z.; Aryana, S.A. Examination of Haines Jump in Microfluidic Experiments via Evolution Graphs and Interface Tracking. Fluids 2022, 7, 256. https://doi.org/10.3390/fluids7080256

[20] Chau, K., Millare, B., Lin, A. et al. Dependence of the quality of adhesion between poly(dimethylsiloxane) and glass surfaces on the composition of the oxidizing plasma. Microfluid Nanofluid 10, 907–917 (2011). https://doi.org/10.1007/s10404-010-0724-y

[21] Rasband, W.S., ImageJ, U. S. National Institutes of Health, Bethesda, Maryland, USA, https://imagej.net/ij/, 1997-2018.

[22] A.F. Stalder, T. Melchior, M. Müller, D. Sage, T. Blu, M. Unser, "Low-Bond Axisymmetric Drop Shape Analysis for Surface Tension and Contact Angle Measurements of Sessile Drops," Colloids and Surfaces A: Physicochemical and Engineering Aspects, 2010.